

# Acoustic Optimization of Supersonic Multi-Stream Nozzles

Dimitri Papamoschou<sup>1</sup>  
*University of California, Irvine, CA 92697-3975*

**The paper presents a framework for the rapid acoustic optimization of three-dimensional, multi-stream nozzles for the propulsion of supersonic aircraft. The framework is based on Reynolds-Averaged Navier Stokes solutions combined with a Design of Experiments approach. The RANS flow field is collapsed to a surface that is expected to contain the strongest contributions to far-field sound emission. Differential noise predictions are enabled by a modified acoustic analogy, with emphasis on the change in effective perceived noise level (EPNL). Response surfaces for EPNL and thrust loss are obtained after parameterization of the nozzle geometry. The optimal configuration was tested experimentally.**

## I. Introduction

Jet noise is one of the issues that needs to be addressed for commercial supersonic flight to become viable and a design tool is needed to systematically design low-noise nozzles. In particular, there is need for rapid prediction of the trends in noise from variation in nozzle geometry for 3D, multi-stream, and unconventional configurations. Such a tool can be used in optimizing the acoustics and aerodynamics of nozzles.

Time-resolved flow prediction methods such as the large-eddy simulation (LES) have progressed to the point where they can provide high-fidelity, time-resolved solutions to the flow field [1]. Combined with surface integral methods, these computations yield far-field noise spectra that are becoming increasingly reliable [2]. However, the high computational cost, long turnaround times, and enormity of data sets associated with LES-based approaches render them impractical for design purposes. There is need for low-order tools that can provide rapid guidance to the designer of exhaust systems regarding their potential to reduce noise. The robustness of such tools hinges on capturing the salient physics of noise generation and noise reduction. Identifying these physical processes is relevant not only to the development of rapid prediction tools but also to the interpretation of the vast data sets generated by experiments and computations.

The predominant low-order modeling tool used today consists of an acoustic analogy coupled with a Reynolds-Averaged Navier Stokes (RANS) solution of the flow field. The original acoustic analogy formulation by Lighthill [3] uses the free-space Green's function and can yield satisfactory results for round jets [4]. Improvements have included the effect of refraction by the mean flow, which requires solving the linearized Euler equations [5,6]. Simplification is often sought through the locally parallel flow approximation, in which case the Green's function can be reduced to analytical forms. This approach has yielded accurate predictions for jets from round nozzles as well as overall-axisymmetric configurations nozzles with chevrons and fluidic injection [7,8,9]. Incorporation of models for the velocity-enthalpy correlation have shown promise in predicting the acoustics of hot jets [10].

For three-dimensional jets, inclusion of refraction effects is of paramount importance as they govern the azimuthal directivity of the sound emission. The computational challenges are thus magnified relative to axisymmetric jets. Even under the simplification of the parallel-flow approximation, the construction of Green's functions involves complex numerical procedures [11]. The parallel-flow approximation itself poses the risk of disregarding flow features that could play a critical role in the generation or suppression of noise [12]. Application of the parallel-flow Green's function approach to three-stream jets with offset tertiary duct has shown a qualitative match of the noise reduction trend; however, quantitatively the

---

<sup>1</sup> Professor, Department of Mechanical and Aerospace Engineering, dpapamos@uci.edu, Fellow AIAA.

asymmetry in the modeled azimuthal directivity was significantly weaker than the experimental one [13,14].

Although the Green's function approach is the most rigorous way to obtain noise predictions for three-dimensional jets, it is fair to say that, at this stage of its development, the inherent numerical complexities and skill level expected of the operator are not compatible with the desired rapid optimization approach. Simpler options that will give the designer guidance in real time, once the RANS solution is available, are desirable.

The current approach is based on the differential noise prediction method of Ref. [15], which is a RANS-based acoustic analogy framework that addresses the noise in the polar direction of peak emission and uses the Reynolds stress as a time-averaged representation of the action of the coherent turbulent structures. The framework preserves the simplicity of the original acoustic analogy formulation by Lighthill, using the free-space Green's function, while accounting for azimuthal effects via special forms for the space-time correlation combined with source-observer relations based on the Reynolds stress distribution in the jet plume.

A central premise in the model is that the sound emission is strongly influenced by the dynamics of the outer shear layer of the multi-stream jet. In a time-averaged sense, we place attention on the outermost peak of the Reynolds stress, resulting in the definition of the outer surface of peak Reynolds stress (OSPS). The mean axial velocity on this surface is thought to best represent the convective velocity of the eddies primarily responsible for peak noise emission. The axial convective Mach number, which controls the radiation efficiency, is defined accordingly. The resulting OSPS and convective Mach number distribution on this surface provide guidance as to the noise reduction potential of a particular nozzle configuration.

The space-time correlation of the Lighthill stress tensor is defined in a fixed frame of reference and comprises axial, timewise, and cross-stream correlations. The axial-timewise formulation is designed to reproduce qualitatively the main features of the axial space-time correlation and uses the aforementioned definition of axial convective velocity. The cross-stream correlation is based on the projected distance between two source elements, a formulation that helps ensure that the modeled power spectral density is real and nonnegative. An important feature is the inclusion of a transverse space-time correlation and associated transverse convective velocity. In conjunction with the Hankel transform of the cross-stream correlation, the transverse propagation induces an azimuthal directivity in the far-field spectral density. It is this effect that replaces, in a qualitative sense, the effect of the Green's functions.

This paper describes UC Irvine's contribution to a broader project on acoustic optimization of multi-stream, 3D nozzles (see the Acknowledgments). In the UCI effort, the method of Ref. 15 was expanded to be applicable to all polar emission angles of relevance to aircraft noise. A collapse of the volume integral over the source region to a surface integral over the OSPS is attempted to provide rapid prediction of the change in the far-field sound pressure level relative to a baseline. The model was parameterized and the parameter vector was inferred from fitting the noise change of existing experiments. The same parameter vector was then used to predict the change in acoustics for new nozzle configurations. The prediction methodology was integrated with a design-of-experiments approach to provide response surfaces used to identify an optimal configuration. This configuration was then tested experimentally.

## **II. Computational and Experimental Methods**

### **A. RANS Solver**

A number of Reynolds-Averaged Navier Stokes (RANS) computations of the internal and external flows of three-stream nozzles were conducted. The computational fluid dynamics code used at UCI is known as PARCAE [16] and solves the unsteady three-dimensional Navier-Stokes equations on structured multiblock grids using a cell-centered finite-volume method. Information exchange for flow computation on

multiblock grids using multiple CPUs is implemented through the MPI (Message Passing Interface) protocol. In its time-averaged implementation, the code solves the RANS equations using the Jameson-Schmidt-Turkel dissipation scheme [17] and the Shear Stress Transport (SST) turbulence model of Menter [18]. The SST model combines the advantages of the  $k-\omega$  and  $k-\varepsilon$  turbulence models for both wall-bounded and free-stream flows.

The governing equations were solved explicitly in a coupled manner using five-stage Runge-Kutta scheme toward steady state with local time stepping, residual smoothing, and multigrid techniques for convergence acceleration. Only the steady-state solution was considered because we are interested in the time-averaged features of the flow. The computation encompassed both the internal nozzle flow as well as the external plume of three-stream nozzles where the primary and secondary streams came into contact internally and exited a common duct of diameter  $D_c$ . With reference the exit of the common nozzle, the axial extent of the computational domain ranged from  $-4 D_c$  to  $40 D_c$ . The radial extent was  $10 D_c$ . As all the configurations were symmetric about the vertical plane, only one-half of the domain was modeled to save computational cost. The typical grid contained 8 million points. The grid was divided into multiblocks to implement parallelization on multiprocessor computers to reduce the convergence time. For the primary, secondary, and tertiary duct flows, uniform total pressure was specified at the inlet surface corresponding to the perfectly expanded exit Mach number. For the ambient region surrounding the nozzle flow, characteristic boundary condition was defined, and the downstream static pressure was set equal to the ambient pressure. Adiabatic no-slip boundary condition was specified on all nozzle walls. Figure 1 shows an illustrative grid for the baseline nozzle MAXI01.

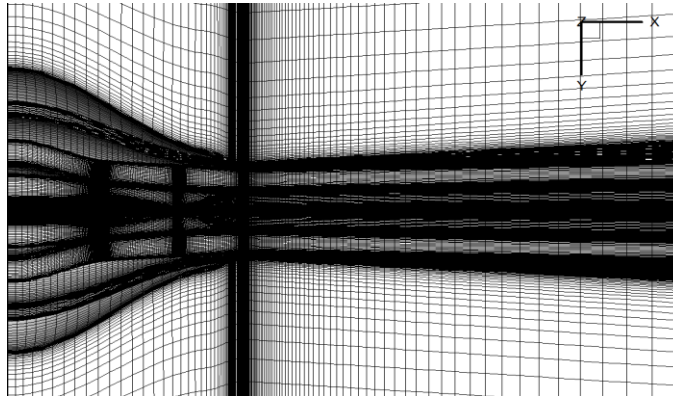


**Fig. 1** Portion of computational mesh used for three-stream coaxial nozzle MAXI01.

The computations were conducted at the scale (Reynolds number) of the UCI experiments and at the conditions listed in Section IV of this report. To facilitate convergence, the ambient Mach number was set to 0.05 (ambient velocity of 17.2 m/s), while the experiments were at static conditions.

## **B. Aeroacoustic Experiments**

### *1. Generic Nozzle Design*

The objective of the nozzle design process was to generate test articles that enabled rapid and accurate testing of a variety of nozzles having characteristics compatible with the exhaust of three-stream, variable-cycle engines envisioned for future supersonic aircraft. The nozzles needed to fit the capacity of the UCI Jet Aeroacoustics Facility, a triple-stream jet facility that delivers helium-air mixtures to the primary, secondary, and tertiary ducts of the nozzle. Helium-air mixtures simulate accurately the acoustics and fluid mechanics of hot jets [19]. The sub-millimeter tolerance requirements for the nozzle exit motivated a design where all the nozzle components are built in one piece, using high-definition stereolithography which allows nozzle lips as thin as 0.2 mm. The material used was Accura 60 plastic (3D Systems) with tensile strength in the range of 58-68 MPa. The design comprises a fixed base on which replaceable nozzle attachments are mounted. Figure 2 depicts the main design features of a representative nozzle. Measurement

of the total pressure of each stream involves thin channels, of 0.75-mm diameter, introduced into support struts in each of the ducts. The channels begin at the outer surface of the attachment, follow an L-shaped path through the struts, and terminate into upstream-facing ports in their respective ducts.

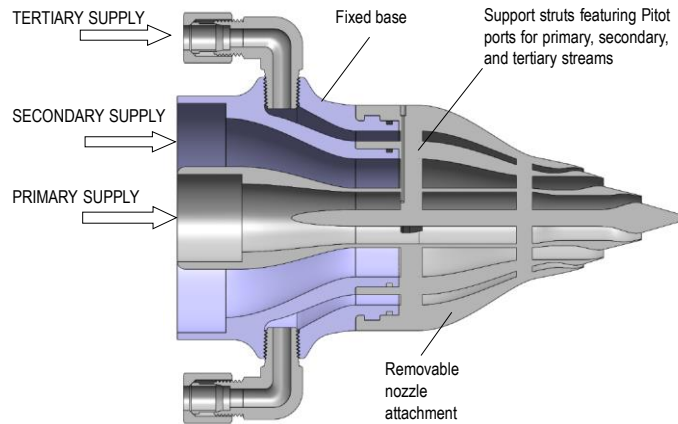


**Fig. 2 Generic design of UCI three-stream nozzle.**

## 2 Acoustic Measurement

Noise measurements were conducted inside an anechoic chamber equipped with up to twenty-four 1/8-in. condenser microphones (Brüel & Kjaer, Model 4138, TEDS) with frequency response up to 120 kHz. Figure 3 shows the layout and a photograph of the facility. Twenty-four microphones on an inclined holder were used to survey a polar angle  $\theta$  range approximately from  $20^\circ$  to  $120^\circ$ . Different azimuthal angles were surveyed by rotating the nozzle. The following azimuthal angles were surveyed:  $\phi = 0^\circ$  (downward),  $30^\circ$ ,  $60^\circ$ , and  $90^\circ$ .

The microphones were connected to conditioning amplifiers (Brüel & Kjaer, Model 2690-A-0S4) whose outputs were sampled simultaneously, at 250 kHz per channel, by multi-function data acquisition boards (National Instruments PCI-6143) installed in a Dell Precision T7400 computer with a Xeon quad-core processor. National Instruments LabView software is used to acquire the signals. The temperature and humidity inside the anechoic chamber are recorded to enable computation of the atmospheric absorption. The microphones are regularly calibrated using a pistonphone.

The microphone signals were conditioned with a high-pass filter set at 300 Hz. Narrowband spectra were computed using a 4096-point Fast Fourier Transform, yielding a frequency resolution of 61 Hz. The spectra were corrected for microphone actuator response, microphone free field response and atmospheric absorption, thus resulting in lossless spectra. The correction for atmospheric absorption utilized the relations in Bass *et al.* [20]. For the typical testing conditions of this experiment, and for the farthest microphone location, the absorption correction was 4.5 dB at 120 kHz. The SPL spectra are referenced to a radius of 12 in. from the nozzle exit.

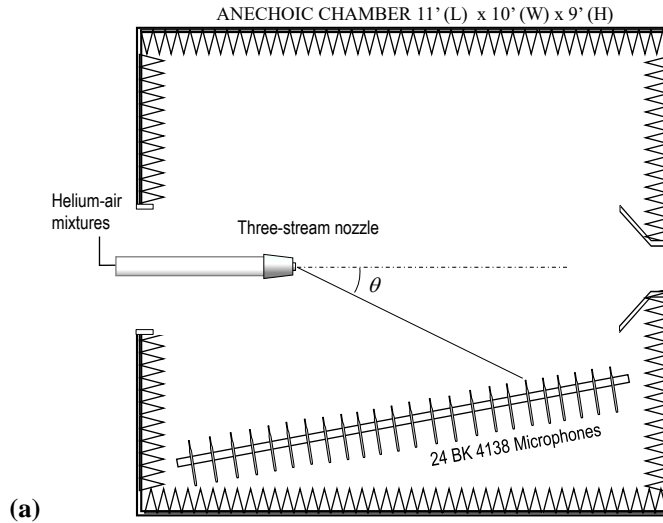


**Fig. 3 (a) Diagram and (b) picture of UCI anechoic chamber and microphone instrumentation.**

### 3. EPNL Estimates

Estimates of Effective Perceived Noise Level (EPNL) were obtained using the method outlined in Ref. 21. Here the basic steps are summarized. Referring to Fig. 4, the flight path is selected to be a piece-wise linear trajectory, at zero altitude until  $x = 0$  and sloped at the climb angle  $\gamma$  for  $x > 0$ . Thus, the lift-off point is defined to be  $x = 0$ . The aircraft travels at constant Mach number  $M_\infty$  and, for  $x > 0$ , constant climb angle  $\gamma$ . The engine axis is at a constant “angle of attack”  $\alpha$  relative to the local direction of the flight path. The coordinates  $(x_a, y_a, 0)$  refer to the actual aircraft position, while  $(x, y, 0)$  are the aircraft coordinates at the retarded time. The observer is located at  $(x_0, 0, z_0)$  where  $z_0$  takes the values 0 m for the takeoff monitor and 450 m for the sideline monitor.

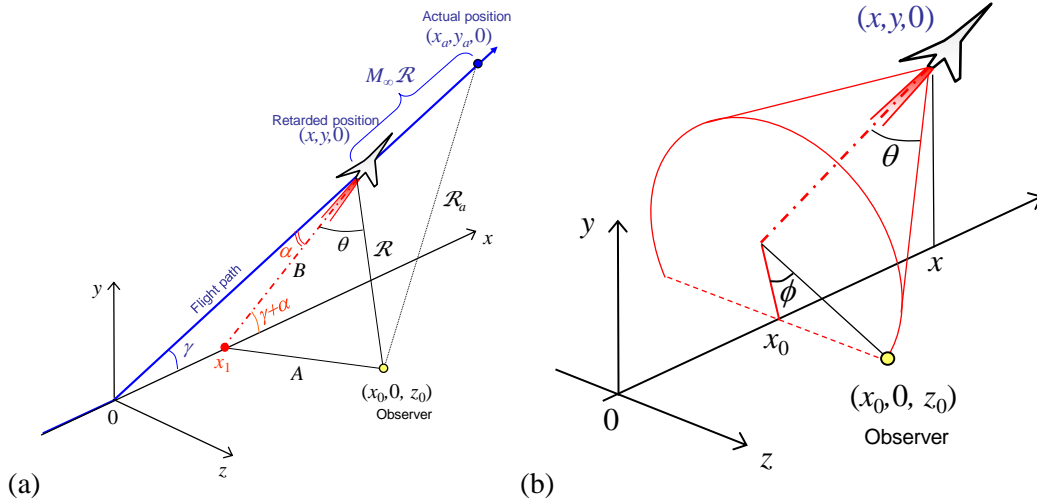


**Fig. 4 (a) Flight path and geometric construction for the polar angle  $\theta$ ; (b) definition of the azimuthal angle  $\phi$ .**

Assuming a scale factor SF that gives the desired full-scale static thrust, the lossless narrowband SPL spectra measured in the subscale experiments are extrapolated to the frequency  $SF \times 20$  kHz, i.e., the highest frequency of the audible spectrum. Here the extrapolation used a roll-off of -15 dB/decade. The EPNL results are very insensitive on this slope. Increasing the slope to -10 dB/decade, for instance, impacted the EPNL predictions by less than 0.05 dB and the EPNL differences by less than 0.02 dB. Following the extrapolation, the frequency is divided by the scale factor. For a given flight path, the following steps are taken to estimate the flyover Perceived Noise Level (PNL) and the Effective Perceived Noise Level.

1. For each time step  $t$  of the retarded airplane location (typically in 0.5-s intervals) the observer polar and azimuthal angles,  $\theta(t)$  and  $\phi(t)$ , are calculated using the geometry of Fig.4. The corresponding SPL spectrum is then selected. This step requires interpolation between spectra and, for polar angles outside the range covered in the experiment, moderate extrapolation. To enhance the accuracy of interpolation or extrapolation the spectra were smoothed using a Savitzky-Golay filter.
2. The spectrum is corrected for distance and atmospheric absorption. The absorption correction is applied for ambient temperature 29°C and relative humidity 70% (conditions of least absorption) using the relations of Bass *et al.* [20].
3. The spectrum is discretized into 1/3-octave bands and the perceived noise level (PNL) is computed according to Part 36 of the Federal Aviation Regulations [22].
4. The PNL is corrected for lateral attenuation according to FAA's INM7.0 [8]. This impacts only the sideline estimate.
5. The previous step gives the time history of perceived noise level, PNL(t). From it, the maximum level of PNL, PNL<sub>M</sub>, is determined. The duration of PNL exceeding PNL<sub>M</sub>-10 dB is calculated and the corresponding "duration correction" is computed according to FAR 36. The effective perceived noise level, EPNL, equals PNL<sub>M</sub> plus the duration correction. The estimate of EPNL includes the "tone correction", a penalty for excessively protrusive tones in the 1/3-octave spectrum, although the present spectra are devoid of such tones.

The flight path selected for the present flyover simulations has the shape depicted in Fig. 4. The time history starts 10 s before the lift off point, which is set at  $x_a = 0$ . The aircraft is traveling at a constant Mach number  $M_\infty = 0.25$ . The climb is performed at angle  $\gamma = 5^\circ$  and the engine angle of attack is set at  $\alpha = 5^\circ$ . The sideline monitor (SL) is located at  $z_0 = 450$  m and at the axial distance where the aircraft's altitude is 305 m (1000

ft), which is a common reference point. The takeoff monitor (TO) is located at  $z_0=0$  m and at the axial distance where the aircraft's altitude is 457.5 m (1500 ft). The scale factor used in the PNL and EPNL estimates is  $SF=40$ , corresponding to a full-scale static thrust of 120 kN (27,000 lb). A twin-engine configuration was considered.

The predictions and optimization in this project focused on the reduction in the “cumulative” EPNL, i.e., the summation of EPNL (in dB) at the takeoff and sideline monitors. This reduction will be symbolized as  $\Delta EPNL_{TO+SL}$ .

### III. Noise Prediction Methodology

#### A. Background

A rapid predictive methodology was developed for the *noise reduction* offered by an asymmetric jet relative to a known axisymmetric (baseline) jet. The methodology encompasses all polar and azimuthal angles of relevance to aircraft noise. It expands on the main elements of the approach of Ref. 15, that is, a RANS-based acoustic analogy framework that addresses the noise in the polar direction of peak emission and uses the Reynolds stress as a time-averaged representation of the action of the coherent turbulent structures. The magnitude of the principal component of the Reynolds stress is modeled as

$$g = \nu_T |\nabla \bar{\mathbf{u}}| \quad (1)$$

where  $\nabla \bar{\mathbf{u}}$  is the mean velocity gradient and  $\nu_T$  is the turbulent viscosity.

A central premise in the model is that the sound emission is strongly influenced by the dynamics of the outer shear layer of the multi-stream jet. In a time-averaged sense, we consider the outermost peak of the Reynolds stress, resulting in the definition of the outer surface of peak Reynolds stress (OSPS). The mean axial velocity represents the convective velocity of the eddies primarily responsible for peak noise emission. The axial convective Mach number, which controls the radiation efficiency, is defined accordingly. The resulting OSPS surface and the distributions on it of convective Mach number,  $M_c$ , Reynolds-stress magnitude  $g$ , turbulent kinetic energy  $k$ , and specific dissipation  $\Omega$  are central elements of the model. Correlation time and length scales,  $\mathcal{T}$  and  $\mathcal{L}$ , respectively, are constructed from  $k$  and  $\Omega$  as will be discussed next. Additional important elements include the azimuthal angle of the mean velocity gradient,  $\phi_g$ , and the transverse convective Mach number  $\mu_c$  that controls the azimuthal directivity. Figure 5 depicts the coordinate system used and related important variables. Azimuthal angles  $\phi$  and radii  $y$  are defined relative to the centroid of the jet, which is selected to be the locus of the maximum mean velocity. The far-field observer is located at polar angle  $\theta_0$  and azimuthal angle  $\phi_0$ .

The model of Ref. 15 was successful in predicting the noise reduction in the direction of peak emission but was not applicable to other polar angles. Here the methodology was extended to all polar angles of relevance by including the effects of self-noise that arises from the fourth-order correlation terms.

#### B. Detection of the Outer Surface of Peak Stress (OSPS)

The detection of the OSPS follows the general guidelines in Ref. 15 with some refinement. The RANS flow field is divided into axial slices of very fine spacing near the nozzle exit and coarser spacing downstream. Each axial slice is divided into fine azimuthal segments, typically in 1.25-degree increments. Within each azimuthal segment, the data (velocity, Reynolds stress) are sorted in order of decreasing radius  $y$ . The search process for the first (outermost) peak of the Reynolds stress starts at the radial location where the mean axial velocity is a fraction (typically 1/4) of the tertiary exit velocity, a position that is well outside the dividing streamline of the outermost shear layer but still within the jet flow. From these outer positions, rays are generated along the mean velocity gradient that propagate inward. The ray propagation stops at

the detection of the first maximum of the Reynolds stress. Thus, the ends of the rays define the location of the OSPS at given axial station. Figure 6 presents examples of this detection scheme.

Denoting the radial location of the OSPS as  $y_{OSPS}(X, \phi)$ , and letting  $\mathbf{y} = (X, y, \phi)$  represent the location of a volume element in polar coordinates, the convective Mach number of that element is defined as

$$M_c(X, y, \phi) = \frac{1}{a_\infty} \bar{u}(X, y_{OSPS}(X, \phi), \phi) \quad (2)$$

where  $\bar{u}$  is the mean axial velocity and  $a_\infty$  is the ambient speed of sound. This means that all the volume elements at a particular  $X$  and  $\phi$  are assigned the same value of  $M_c$  as determined by Eq. 2.

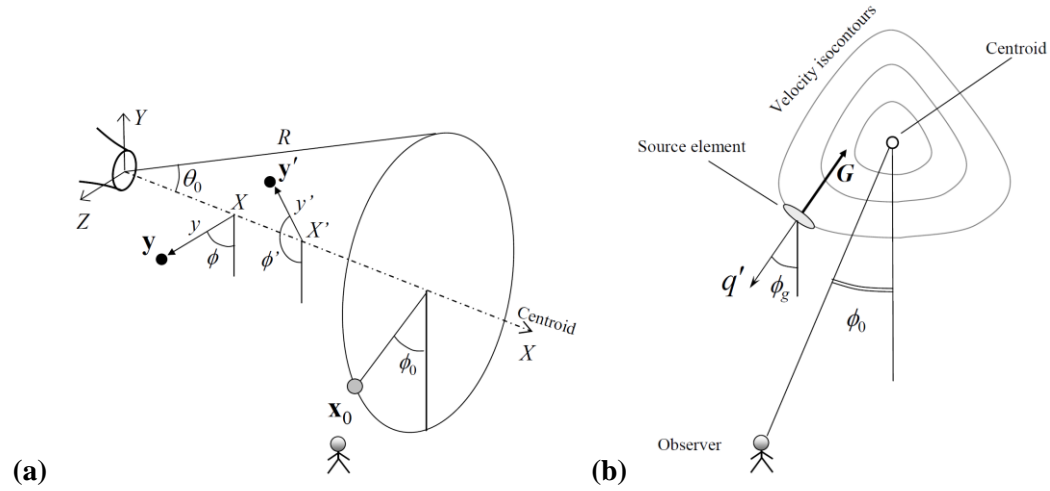


**Fig. 5 (a) Coordinate systems used in acoustic analogy model; (b) quantities on a cross-stream plane. From Ref. 9**

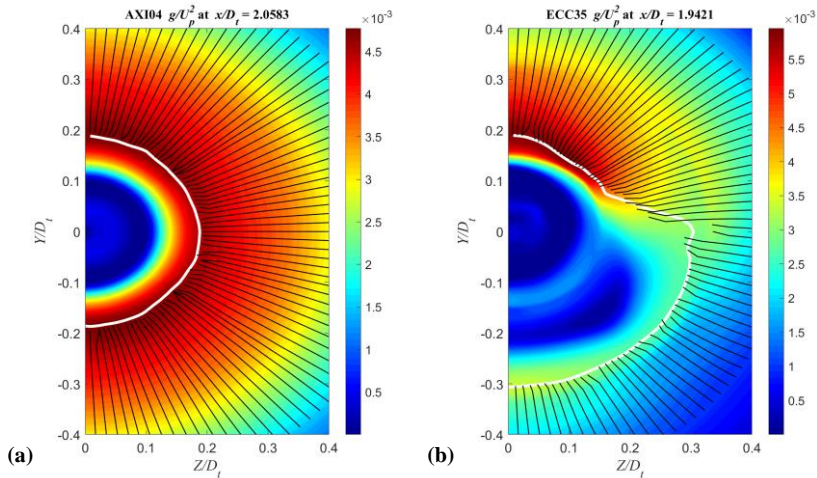


**Fig. 6. Examples of detection of the outer surface of peak Reynolds stress (OSPS) on cross-sectional planes of three-stream jets. Contours represent the Reynolds stress  $g$ . Black lines are the rays used to detect the outermost peak of  $g$ . White lines are the resulting OSPS. (a) Axisymmetric jet; (b) asymmetric jet.**

### C. Inclusion of Self-Noise Contribution

The model of Ref. 15 was developed using only the second-order correlations of the Lighthill stress tensor, which comprise the shear-noise component of the radiated noise. The fourth-order correlations pertinent to self noise were included here by using the quasi-normal hypothesis

$$\overline{u'_i u'_j u'_k u'_l} = \overline{u'_i u'_k} \overline{u'_j u'_l} + \overline{u'_i u'_l} \overline{u'_j u'_k} \quad (3)$$

and the dimensional constructs found in Ref.15. The resulting terms and their directivities are listed in Table 1, together with those of shear noise.

Table 1 Distinct terms of  $A_{ijkl}$  and associated directivities

$A_{ijkl}$	Mult.	Expression		Approximation		Directivity $\vartheta_i \vartheta_j \vartheta_k \vartheta_l$
		$\frac{A_{ijkl, \text{shear}}}{\overline{p^2 \overline{u^2}}}$	$\frac{A_{ijkl, \text{self}}}{\overline{p^2}}$	$\frac{A_{ijkl, \text{shear}}}{\overline{p^2 \overline{u^2}}}$	$\frac{A_{ijkl, \text{self}}}{\overline{p^2}}$	
$A_{1111}$	1	$4\overline{u'u'}$	$2\overline{u'u'^2}$	$\frac{8}{3}k$	$\frac{8}{9}k^2$	$\cos^4 \theta_0$
$A_{1112}$	4	$2\overline{u'v'}$	$2\overline{u'u'} \overline{u'v'}$	$-2g \cos \phi_g$	$-\frac{4}{3}kg \cos \phi_g$	$-\cos^3 \theta_0 \sin \theta_0 \cos \phi_0$
$A_{1113}$	4	$2\overline{u'w'}$	$2\overline{u'u'} \overline{u'w'}$	$2g \sin \phi_g$	$\frac{4}{3}kg \sin \phi_g$	$\cos^3 \theta_0 \sin \theta_0 \sin \phi_0$
$A_{1122}$	2	0	$2\overline{v'v'^2}$	0	$2g^2 \cos^2 \phi_g$	$\frac{1}{4} \sin^2(2\theta_0) \cos^2 \phi_0$
$A_{1123}$	4	0	$2\overline{v'v'} \overline{u'w'}$	0	$-g^2 \sin(2\phi_g)$	$-\frac{1}{8} \sin^2(2\theta_0) \sin(2\phi_0)$
$A_{1133}$	2	0	$2\overline{w'w'^2}$	0	$2g^2 \sin^2 \phi_g$	$\frac{1}{4} \sin^2(2\theta_0) \sin^2 \phi_0$
$A_{1212}$	4	$\overline{v'v'}$	$\overline{u'u'} \overline{v'v'} + \overline{u'v'^2}$	$\frac{2}{3}k$	$\frac{4}{9}k^2 + g^2 \cos^2 \phi_g$	$\frac{1}{4} \sin^2(2\theta_0) \cos^2 \phi_0$
$A_{1213}$	8	$\overline{v'w'}$	$\overline{u'u'} \overline{v'w'} + \overline{u'v'} \overline{u'w'}$	0	$0 - \frac{1}{2}g^2 \sin(2\phi_g)$	$-\frac{1}{8} \sin^2(2\theta_0) \sin(2\phi_0)$
$A_{1222}$	4	0	$2\overline{v'v'} \overline{v'v'}$	0	$-\frac{4}{3}kg \cos \phi_g$	$-\cos \theta_0 \sin^3 \theta_0 \cos^3 \phi_0$
$A_{1223}$	8	0	$\overline{u'v'} \overline{v'w'} + \overline{v'v'} \overline{u'w'}$	0	$0 + \frac{2}{3}kg \sin \phi_g$	$\cos \theta_0 \sin^3 \theta_0 \cos^2 \phi_0 \sin \phi_0$
$A_{1233}$	4	0	$2\overline{u'w'} \overline{v'w'}$	0	0	$-\cos \theta_0 \sin^3 \theta_0 \cos \phi_0 \sin^2 \phi_0$
$A_{1313}$	4	$\overline{w'w'}$	$\overline{u'u'} \overline{w'w'} + \overline{u'w'^2}$	$\frac{2}{3}k$	$\frac{4}{9}k^2 + g^2 \sin^2 \phi_g$	$\frac{1}{4} \sin^2(2\theta_0) \sin^2 \phi_0$
$A_{1322}$	4	0	$2\overline{u'v'} \overline{v'w'}$	0	0	$-\cos \theta_0 \sin^3 \theta_0 \cos^2 \phi_0 \sin \phi_0$
$A_{1323}$	8	0	$\overline{u'w'} \overline{v'w'} + \overline{w'w'} \overline{u'v'}$	0	$0 - \frac{2}{3}kg \cos \phi_g$	$-\cos \theta_0 \sin^3 \theta_0 \sin^2 \phi_0 \cos \phi_0$
$A_{1333}$	4	0	$2\overline{w'w'} \overline{u'w'}$	0	$\frac{4}{3}kg \sin \phi_g$	$\cos \theta_0 \sin^3 \theta_0 \sin^3 \phi_0$
$A_{2222}$	1	0	$2\overline{v'v'^2}$	0	$\frac{8}{9}k^2$	$\sin^4 \theta_0 \cos^4 \phi_0$
$A_{2223}$	4	0	$2\overline{v'v'} \overline{v'w'}$	0	0	$-\sin 4\theta_0 \cos^3 \phi_0 \sin \phi_0$
$A_{2233}$	2	0	$2\overline{v'w'^2}$	0	0	$\frac{1}{4} \sin^4 \theta_0 \sin(2\phi_0)$
$A_{2323}$	4	0	$\overline{v'w'^2} + \overline{v'v'} \overline{w'w'}$	0	$0 + \frac{4}{9}k^2$	$\sin^4 \theta_0 \cos^2 \phi_0 \sin^2 \phi_0$
$A_{2333}$	4	0	$2\overline{w'w'} \overline{v'w'}$	0	0	$-\sin^4 \theta_0 \sin^2 \phi_0 \cos \phi_0$
$A_{3333}$	1	0	$2\overline{w'w'^2}$	0	$\frac{8}{9}k^2$	$\sin^4 \theta_0 \sin^4 \phi_0$

### D. Model for the Spectral Density

The model of Ref. 15 for the far-field spectral density  $S$  can be expressed as the volume integral

$$S = \frac{1}{(4\pi\mathcal{R})^2} \left(\frac{\omega}{a_\infty}\right)^4 \int_V A_{0000} Q \hat{R}_1 \hat{R}_4 \tilde{R}_{23} d^3 \mathbf{y} \quad (4)$$

Here  $\omega$  is the radian frequency;  $a_\infty$  is the ambient speed of sound;  $\mathcal{R}$  is the observer distance;  $A_{0000}$  is the amplitude of the correlation of the Lighthill stress tensor in the direction of the observer;  $Q$  is the 4-dimensional correlation volume;  $\hat{R}_1$  and  $\hat{R}_4$  are the Fourier transforms of the axial and timewise components of the space-time correlation of the Lighthill stress tensor; and  $\tilde{R}_{23}$  is the Hankel transform of the cross-

stream correlation. Importantly,  $\hat{R}_1$  contains the radiation efficiency that is controlled by the convective Mach number  $M_c$ , and  $\tilde{R}_{23}$  contains the azimuthal directivity. Integration is done over the volume  $\mathcal{V}$  of the noise source region. For brevity, the arguments of the functions in the integrand are omitted. They will be presented in the next section.

It is now surmised that the *noise change* from a known baseline is primarily due to changes in the constituents of Eq. 4 on the OSPS. Accordingly, we consider a ‘‘collapse’’ of the integral of Eq. 4 on the OSPS, yielding a reduced spectral density

$$\mathbb{S} = \frac{1}{(4\pi R)^2} \left(\frac{\omega}{a_\infty}\right)^4 \int_{OSPS} A_{0000} Q \hat{R}_1 \hat{R}_4 \tilde{R}_{23} d^2 \mathbf{y} \quad (5)$$

The reduced spectral density is not expected to match the actual spectral density of the jet. However, the hope is that it can be used in a *comparative* sense by yielding the change in sound pressure level,

$$\Delta \text{SPL} = 10 \log_{10} \left( \frac{\mathbb{S}}{\mathbb{S}_{base}} \right) \quad (6)$$

where ‘‘base’’ represents the baseline jet. The collapse in Eq. 5 is motivated primarily by the need for rapid evaluation of  $\Delta \text{SPL}$ . In principle, the full integral of Eq. 4 could be used in the methodology that follows. However, the computational demands for parameterization and optimization could be prohibitively expensive.

### E. Evaluation of the Spectral Density

This section provides specific guidance for the evaluation Eq. 5. All the correlations have the stretched-exponential form

$$R_j(t) = \exp(-|t|^{\beta_j}) \quad (7)$$

where  $j=1, 23$ , and  $4$  for the axial, cross-stream, and timewise correlations, respectively. The powers  $\beta_1$  and  $\beta_4$  are free parameters that can range between 0.7 and 2; while  $\beta_{23}$  is set to either 1 (exponential) or 2 (Gaussian). The Fourier transforms of  $R_1$  and  $R_4$  need to be computed numerically. Their arguments are:

$$\hat{R}_1 = \hat{R}_1 \left[ \frac{\omega}{a_\infty} \mathcal{L}_1 \left( \frac{1}{M_c} - \cos \theta_0 \right) \right] \quad (8)$$

$$\hat{R}_4 = \hat{R}_4[\omega \mathcal{T}] \quad (9)$$

The Hankel function of the cross-stream correlation takes the analytical forms:

$$\tilde{R}_{23} = \left\{ 1 + \frac{1}{4} \left( \frac{\omega}{a_\infty} \mathcal{L}_{23} \right)^2 \left[ \sin^2 \theta_0 + \frac{1}{\mu_c^2} - 2 \frac{\sin \theta_0}{\mu_c} \cos(\phi - \phi_0) \right] \right\}^{-3/2}, \quad \beta_{23} = 1 \quad (10a)$$

$$\tilde{R}_{23} = \exp \left\{ -\frac{1}{4} \left( \frac{\omega}{a_\infty} \mathcal{L}_{23} \right)^2 \left[ \sin^2 \theta_0 + \frac{1}{\mu_c^2} - 2 \frac{\sin \theta_0}{\mu_c} \cos(\phi - \phi_0) \right] \right\}, \quad \beta_{23} = 2 \quad (10b)$$

The 4D correlation volume is

$$Q = \mathcal{T} \mathcal{L}_1 \pi \mathcal{L}_{23}^2 \quad (11)$$

The amplitude of the correlation has different forms for shear noise and self noise, arising from the summation of the corresponding contributions in Table 1. Within multiplicative constants, the amplitudes for shear noise and self noise are given respectively by

$$\frac{A_{0000, shear}}{\bar{\rho}^2 \bar{u}^2} = \frac{8}{3} k \cos^2 \theta_0 + 8g \cos^3 \theta_0 \sin \theta_0 \cos(\phi_g - \phi_0) \quad (12)$$

and

$$\frac{A_{0000,self}}{\bar{\rho}^2} = \frac{8}{9}k^2 + \frac{8}{3}kg \sin(2\theta_0) \cos(\phi_g - \phi_0) + 2g^2 \sin^2(2\theta_0) \cos^2(\phi_g - \phi_0) \quad (13)$$

The RANS-based length and time scales are generated using the common constructs

$$L_1 = C_1 \frac{\sqrt{k}}{\Omega} \quad (14)$$

$$L_{23} = C_{23} \frac{\sqrt{k}}{\Omega} \quad (15)$$

$$\mathcal{T} = C_4 \frac{1}{\Omega} \quad (16)$$

The coefficients  $C_1$ ,  $C_{23}$ , and  $C_4$  are treated as free parameters. The turbulent viscosity is determined by the usual dimensional construct

$$\nu_T = C_\mu \frac{k}{\Omega} \quad (17)$$

with  $C_\mu=0.09$ .

The transverse convective Mach number  $\mu_c$  in Eqs. 10 controls the azimuthal directivity of noise emission. For the jets of this study and similar jets, the azimuthal directivity peaks when  $\mu_c \sim 2$ . As  $\mu_c$  becomes large, it is evident from Eqs. 10 that emission becomes more uniform with azimuthal angle. Based on past experience, this directivity is expected to be strong for polar angles near the direction of peak emission and weak for high polar angles. Accordingly, an empirical formulation for  $\mu_c$  is constructed as follows:

$$\mu_c(\theta_0, \omega) = \mu_{c,peak} \exp\left\{[C_\theta |\theta_0 - \theta_{peak}(\omega)|]^{\beta_5}\right\} \quad (18)$$

where  $\theta_{peak}(\omega)$  is the angle of peak emission of the baseline far-field spectral density.  $\mu_{c,peak}$ ,  $C_\theta$ , and  $\beta_5$  are free parameters.

The spectral-density contributions of shear noise and self noise are added incoherently in the form

$$S_{tot} = S_{shear} + \alpha S_{self} \quad (19)$$

where the amplitude ratio  $\alpha$  is an additional free parameter. The respective amplitudes are given by Eqs.12 and 13. The two components of noise share the same free parameters  $\mu_{c,peak}$ ,  $C_\theta$ , and  $\beta_5$ . The free parameters  $C_1$ ,  $C_{23}$ ,  $C_4$ ,  $\beta_1$ , and  $\beta_4$  are allowed to be different for each type of noise. For the cross-stream correlation, best results have been obtained with  $\beta_{23} = 2$  for shear noise and  $\beta_{23} = 1$  for self noise. This means that the Hankel transform of the cross-stream correlation has the form of Eq.10a for self noise and Eq. 10b for shear noise.

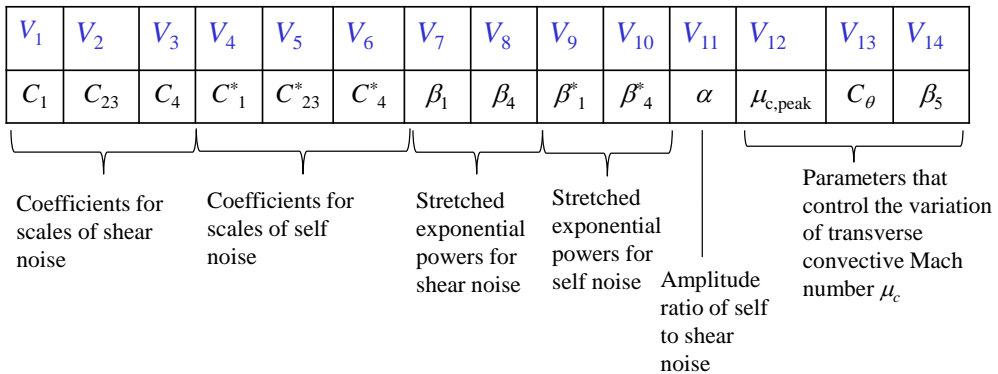


**Fig. 7 Definition of parameter vector V.**

## F. Definition of Parameter Vector

The free parameters defined in the previous section are collected in a parameter vector  $\mathbf{V}$  that controls the modeled  $\Delta\text{SPL}$ . The vector has 14 components, as shown in Fig. 7.

Knowledge of the parameter vector enables evaluation of the modeled  $\Delta\text{SPL}$  for all polar and azimuthal of interest. In the following, this will be referred to as  $\Delta\text{SPL}_{\text{mod}}(\mathbf{V})$ .

## G. EPNL Considerations

In determining the parameter vector, it is important to consider which part of  $\Delta\text{SPL}(\omega, \theta)$  has the strongest influence on the effective perceived noise level (EPNL). The implication is that the parameter vector is determined for the part of the spectrum (in frequency – polar angle space) that is most influential to aircraft noise and unnecessary effort is not expended trying to match parts of the spectrum that are irrelevant. This of course will depend on the type of engine used and the flight profile. Here the EPNL calculation was based on the specifications given in Section IV. The process used to determine the EPNL sensitivity is illustrated in Fig. 8. To assess the sensitivity of EPNL on spectral changes, a spectral “bump” is added to the baseline spectrum. The bump is Gaussian in  $\log(\omega)$  and  $\theta$ . It is swept incrementally over the entire  $\omega$  -  $\theta$  map of relevance to aircraft noise and the change in EPNL is computed for each bump location (typically  $10 \times 10 = 100$  bump locations were used). The resulting change in EPNL, illustrated in Figs. 8a and b, is then used as a weighting factor for  $\Delta\text{SPL}$ . In the example of Fig. 8, the bump amplitude was  $-3$  dB. The baseline spectrum peaks at lab frequency  $f = 3$  kHz and  $\theta = 25^\circ$ . The maps of Fig. 8 show that the EPNL is most sensitive to frequencies near 8 kHz (about 2.5 times the frequency of peak emission) and  $\theta = 30^\circ$ . Very little contribution comes from  $\theta \geq 80^\circ$ .

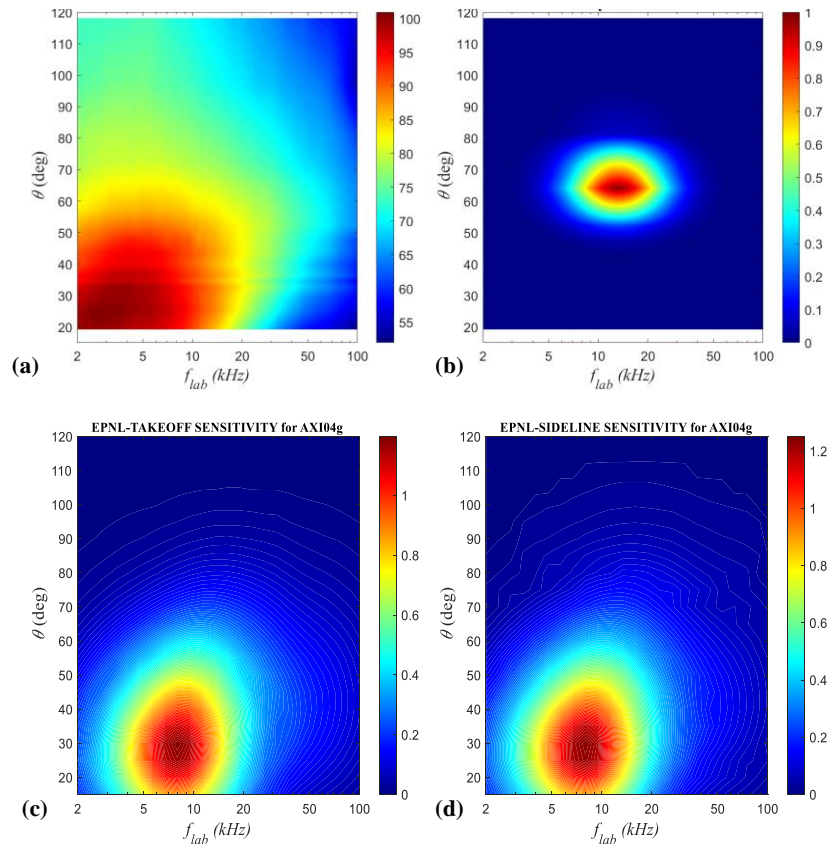


**Fig. 8 EPNL sensitivity. (a) Baseline SPL spectrum (dB) of three-stream jet AXI04U in lab frequency – polar angle map; (b) normalized amplitude of localized bump in SPL, shown at a sample location; (c) and (d): changes in takeoff and sideline EPNL, respectively, versus location of the bump.**

The  $\Delta$ EPNL results are fairly insensitive to the bump amplitude and bump width, as long as the width is much smaller than the extent of the  $\omega$ - $\theta$  map. This exercise is considered as useful guidance as to which part of the spectrum is relevant to aircraft noise for a particular engine and aircraft takeoff profile. For instance, changing the angle of attack and/or climb angle will shift the polar location of peak EPNL sensitivity. The analysis considered only axisymmetric configurations and changes, but can be extended to bumps with finite azimuthal extent. The EPNL-weighted  $\Delta$ SPL will be denoted  $\Delta$ SPL<sup>w</sup> in the analysis that follows.

## H. Determination of the Parameter Vector

The parameter vector  $\mathbf{V}$  is estimated by minimizing the difference between the modeled and experimental  $\Delta$ SPL of relevance to EPNL. Accordingly, we define the cost function

$$F(\mathbf{V}) = \left\| \Delta\text{SPL}_{\text{mod}}^w(\mathbf{V}) - \Delta\text{SPL}_{\text{exp}}^w \right\| \quad (20)$$

The  $L_2$  norm is evaluated over:

- A number of baseline – eccentric pairs where the experimental SPL and RANS-based OSPS data were available.
- A vector of polar angles of relevance to perceived noise.
- A vector of azimuthal angles of relevance to perceived noise.
- A vector of frequencies (Strouhal numbers) of relevance to perceived noise.

Equation 20 can then be written explicitly as

$$F(\mathbf{V}) = \sqrt{\frac{1}{N_p N_\omega N_\theta N_\phi} \sum_{i=1}^{N_p} \sum_{j=1}^{N_\omega} \sum_{k=1}^{N_\theta} \sum_{l=1}^{N_\phi} \left[ \Delta\text{SPL}_{\text{mod},i}^w(\mathbf{V}; \omega_j, \theta_k, \phi_l) - \Delta\text{SPL}_{\text{exp},i}^w(\omega_j, \theta_k, \phi_l) \right]^2} \quad (21)$$

In the present assessment, three baseline-eccentric pairs ( $N_p=3$ ) were used, accessing results of past investigations at UCI. The pairs featured different nozzle geometries and cycle conditions. The frequency vector used 10 elements ( $N_\omega=10$ ) that were logarithmically spaced. The polar angle vector comprised 10 equally-space elements ( $N_\theta=10$ ) and the azimuthal-angle vector consisted of four equally-spaced elements ( $N_\phi=4$ ). For each value of the parameter vector  $\mathbf{V}$ , the reduced spectral density of Eq. 5 was evaluated for  $N_p N_\omega N_\theta N_\phi = 1200$  combinations of OSPS-surface pairs, frequencies, polar angles, and azimuthal angles. Minimization of the cost function was done using the conjugate-gradient method of Shanno and Phua [10]. The architecture of the code used in this process is depicted in Fig. 9.

Figure 10 shows results of the parameterization in the forms of contours of  $\Delta$ SPL( $\omega, \theta$ ) for each baseline-eccentric pair and for the azimuthal angles considered here. The frequency is presented in the non-dimensional form of Strouhal number  $Sr = f D_t / U_p$  where  $D_t$  is the tertiary exit diameter and  $U_p$  is the primary exit velocity. The nozzle geometries and OSPS surfaces with  $M_c$  contours are included, and the exhaust conditions are listed. Jet ECC12U (with AXI04U the baseline) featured an aggressive asymmetry that combined eccentricity in the secondary and tertiary ducts. Jet ECC36U (also with AXI04U as baseline) had asymmetry only in the annulus of the tertiary duct. Jet ECC04U (with AXI02U as baseline) had a moderate asymmetry of the tertiary duct only and was delivered at much lower velocities than the previous two jets. All these jets were studied in previous research efforts and their nozzles featured separate-flow exhausts with external plug. This is in contrast to the nozzles of the current study that involve internal mixing of the primary and secondary streams and an internal plug.

The parameter vector that emerged from the aforementioned minimization procedure is listed in Table 2. The overall error was 1.8 dB. Individual errors are shown in Fig. 10.

**Table 2: Parameter Vector Values**

$V_1$	$V_2$	$V_3$	$V_4$	$V_5$	$V_6$	$V_7$	$V_8$	$V_9$	$V_{10}$	$V_{11}$	$V_{12}$	$V_{13}$	$V_{14}$
$C_1$	$C_{23}$	$C_4$	$C^*_1$	$C^*_{23}$	$C^*_4$	$\beta_1$	$\beta_4$	$\beta^*_1$	$\beta^*_4$	$\alpha$	$\mu_{c,peak}$	$C_\theta$	$\beta_5$
5.26	7.64	0.34	2.09	2.85	0.15	0.71	1.86	1.59	0.71	2.05	1.95	1.62	1.55

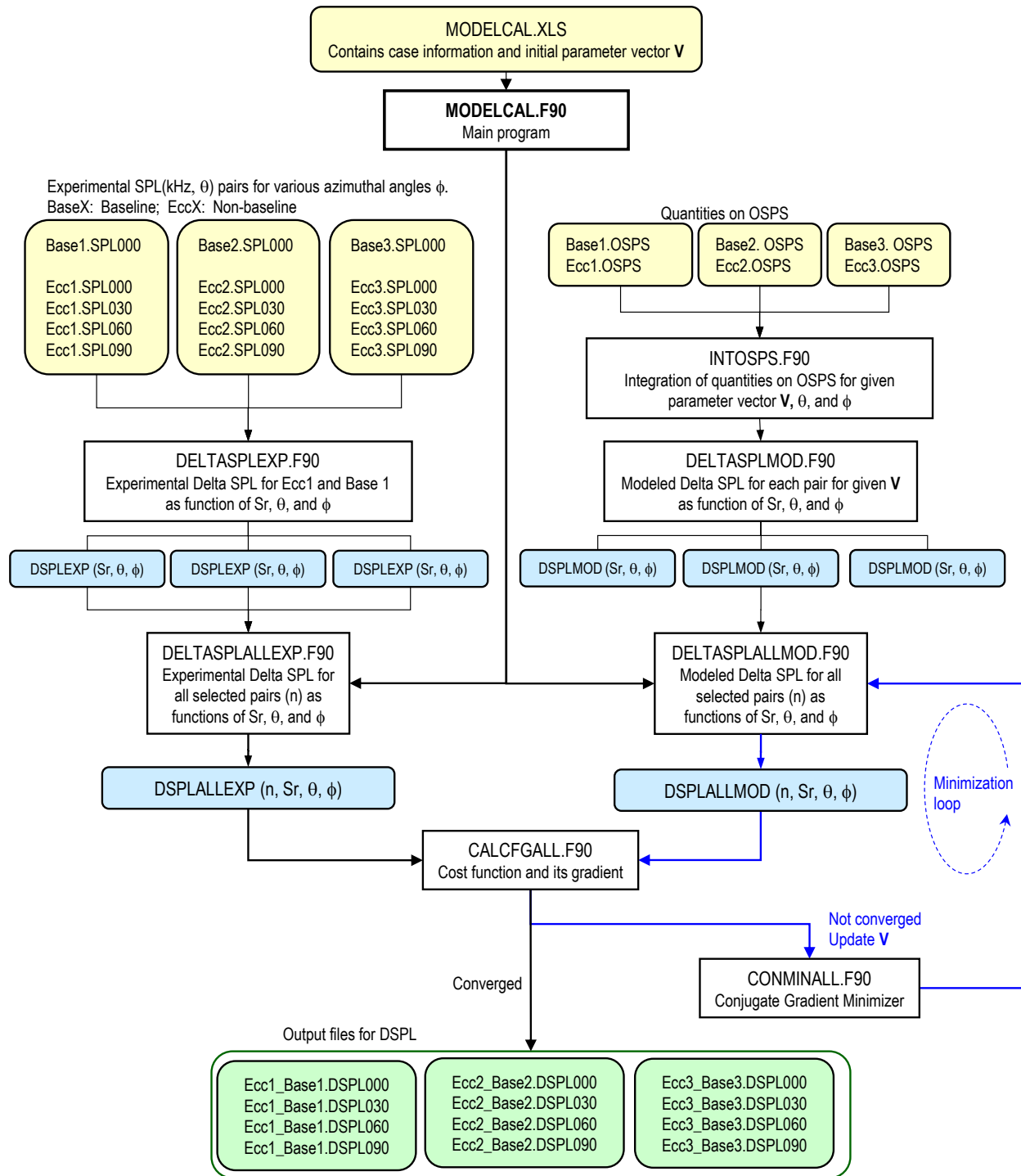
### I. Synthetic SPL Spectra

Once the parameter vector is known, the sound pressure level spectrum for an asymmetric jet is predicted from the spectrum of the corresponding baseline axisymmetric jet plus the modeled  $\Delta\text{SPL}$ , i.e.,

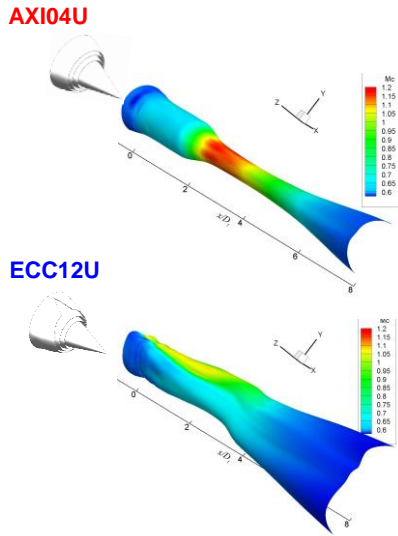
$$\text{SPL}(\omega, \theta, \phi) = \text{SPL}_{\text{base}}(\omega, \theta) + \Delta\text{SPL}_{\text{mod}}(\mathbf{V}, \omega, \theta, \phi) \quad (21)$$

We will refer to this as the “synthetic” SPL spectrum. The baseline and synthetic jet spectra are referenced to a specific radius from the nozzle exit. They can be propagated to an arbitrary far-field location using spherical spreading. Therefore, given a flight path, perceived noise level histories  $\text{PNL}(t)$ , and the difference in effective perceived noise level,  $\Delta\text{EPNL}$ , can be estimated using the relations in Section II.B.3.

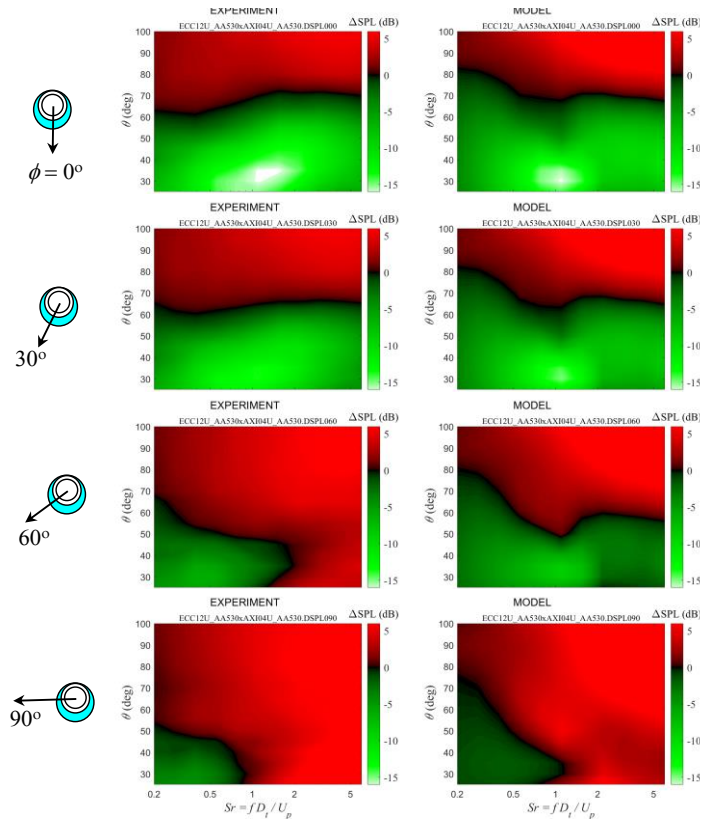
Figure 11 plots synthetic spectra for jet ECC36U. Their similarity with the actual spectra is evident. The model moderately overpredicts the benefit at large azimuthal angle.



**Fig. 9 High-level overview of program structure for predicting  $\Delta$ SPL based on the distribution of RANS variables on the OSPS. The parameter vector  $V$  is determined by matching in a least-squares sense the  $\Delta$ SPL of a number of baseline-eccentric pairs. The pairs in this illustration are Base1-Ecc1, Base2-Ecc2, and Base3-Ecc3.**



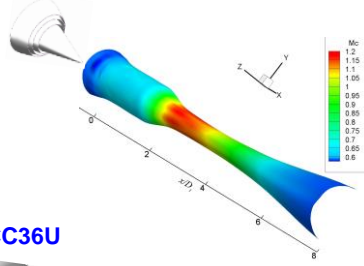
Cycle AA530 (BPR=3.6)	
Stream	Velocity (m/s)
Primary	590
Secondary	370
Tertiary	281



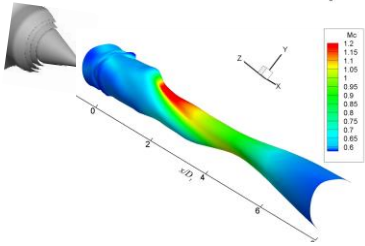
Error = 2.12 dB

Fig. 10 Contour maps of  $\Delta$ SPL (dB) versus Strouhal number  $Sr$  and polar angle  $\theta$  for baseline-eccentric jet pairs. Negative levels (green) indicate noise reduction. Left column: experiment; right column: model. (a) Jet ECC12U with jet AXI04U as the baseline.

AXI04U



ECC36U



Cycle AA530 (BPR=3.6)	
Stream	Velocity (m/s)
Primary	590
Secondary	370
Tertiary	281

$\phi = 0^\circ$

$30^\circ$

$60^\circ$

$90^\circ$

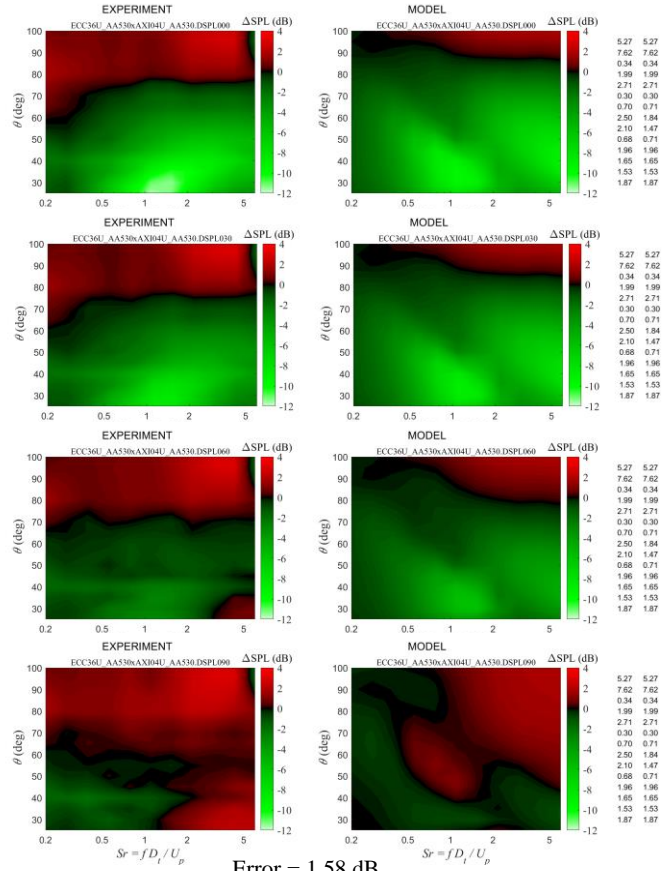
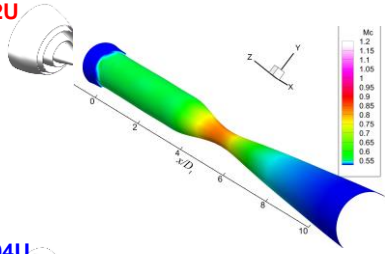


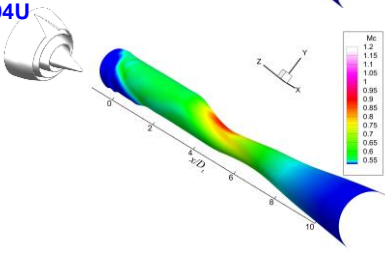
Fig. 10 – continued. (b) Jet ECC36U with jet AXI04U as the baseline.

AXI02U

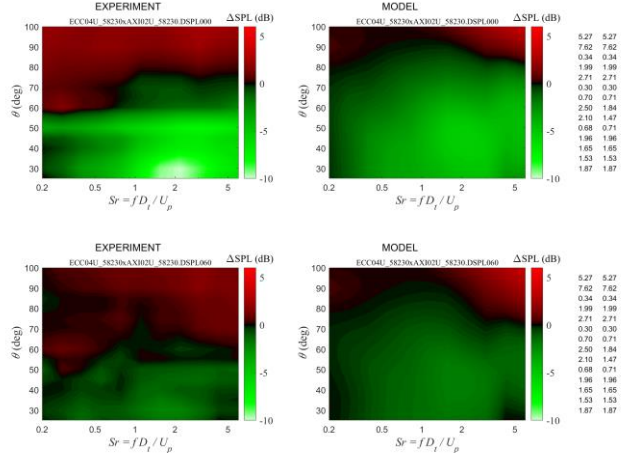


$\phi = 0^\circ$

ECC04U



$60^\circ$



Error = 1.41 dB

Cycle 58230 (BPR=5.8)	
Stream	Velocity (m/s)
Primary	429
Secondary	328
Tertiary	188

Fig. 10 – continued. (c) Jet ECC04U with jet AXI02U as the baseline

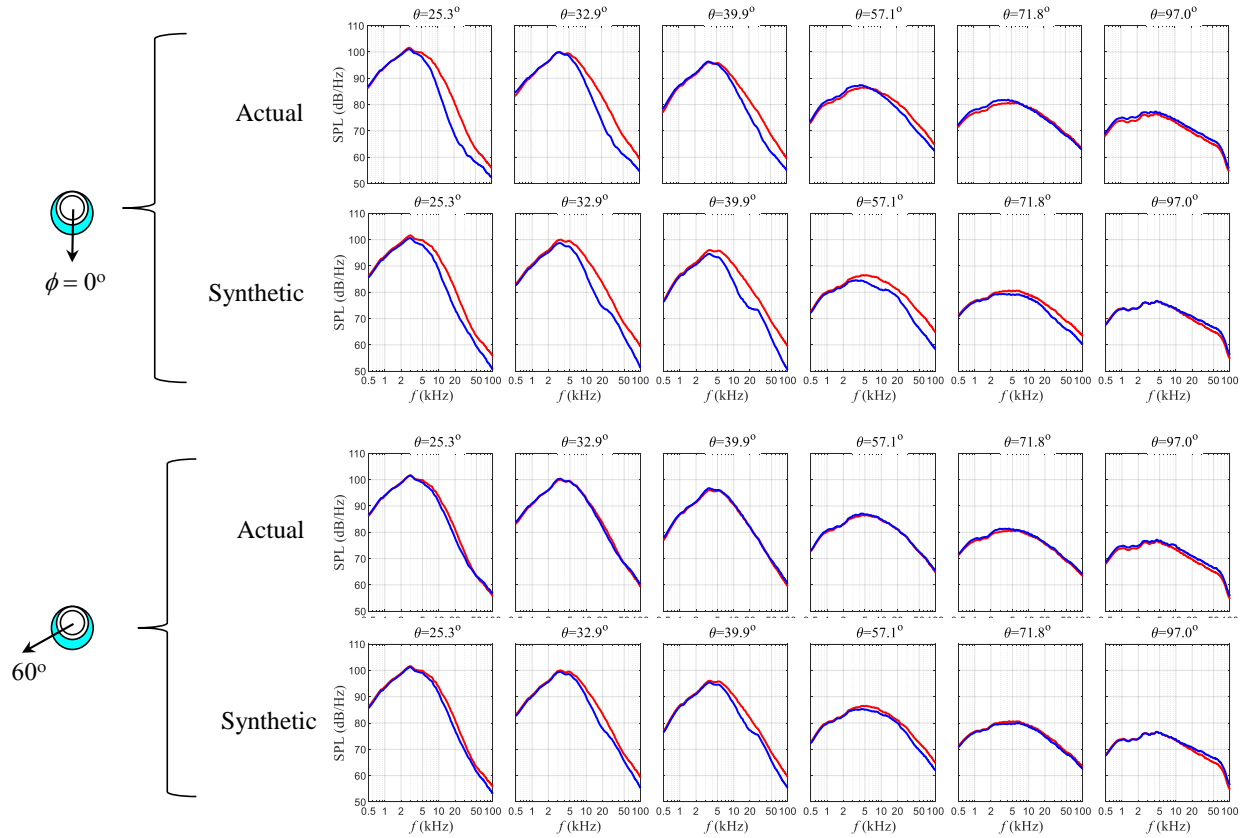


**Fig. 11 Actual and synthetic SPL spectra for jet ECC36U (blue lines) compared to spectra of baseline jet AXI04U (red lines).**

## IV. Nozzle Design and Engine Cycle

### A. General Concept

The nozzle concept considered is that of a three-stream nozzle with internal termination of the secondary duct, as depicted schematically in Fig. 12. The third stream is always separate (unmixed), while the primary and secondary streams can interact internally and exhaust through a common nozzle under the following conditions:

- Unforced mixing. This is close to the operation of separate primary and secondary flows. Limited mixing occurs between the primary and secondary streams.
- Forced mixing. A lobed mixer enhances the mixing between the primary and secondary streams, reflecting the common configuration of internally-mixed turbofans. The exhaust will be vigorously mixed but still non-uniform.
- Fully-mixed equivalent. This is the idealized case where the primary and secondary streams are fully mixed with a uniform exit profile. Experimentally and computationally it is achieved by setting identical total (reservoir) conditions for the primary and secondary streams, at a set point that represents the fully-mixed equivalent condition. Essentially, the nozzle operates as a two-stream nozzle.

This paper concerns configuration (a) only. Noise reduction came by reshaping the duct of the separate tertiary stream.

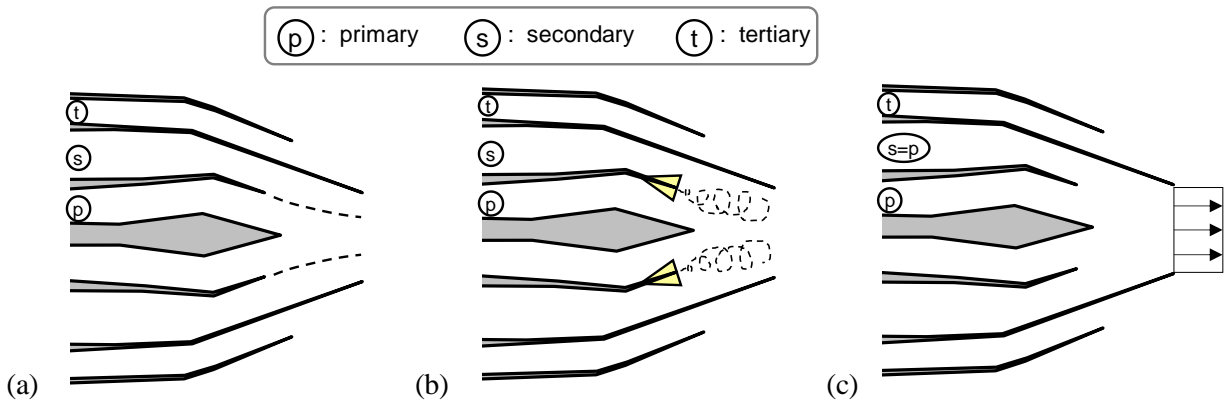


**Fig. 12 Three-stream nozzle concept with internal termination of primary duct. Interaction between primary and secondary streams: (a) unforced mixing; (b) forced mixing using lobed mixer; (c) fully-mixed equivalent (two-stream nozzle).**

### B. Engine Cycle

A high-level thermodynamic analysis of a three-stream turbofan was conducted to evaluate the performance and conditions (Mach numbers, velocities, areas) at critical stations of the nozzle. The following constraints were followed:

- Fan pressure ratio (FPR) not to exceed  $\sim 1.8$  to enable the simplicity of a single-stage fan. Nozzle pressure ratios, in general, should not exceed 2.0.

- Total bypass ratio ( $BPR_{tot}$ ) not to exceed  $\sim 3.5$  to maintain small engine cross-sectional area for supersonic efficiency and low sonic boom signature.
- Nozzle temperature ratio not to exceed  $\sim 4.0$  or, equivalently, fully-mixed velocity not to exceed 1500 ft/s (457 m/s) for Stage 5 compliance.

The analysis considered a maximum rotor (turbine) inlet temperature  $RIT = 1900^{\circ}K$  and an overall pressure ratio  $OPR = 25$ . Figure 13 depicts the thermodynamics models for an unmixed engine and an engine where the primary and secondary streams are internally mixed.

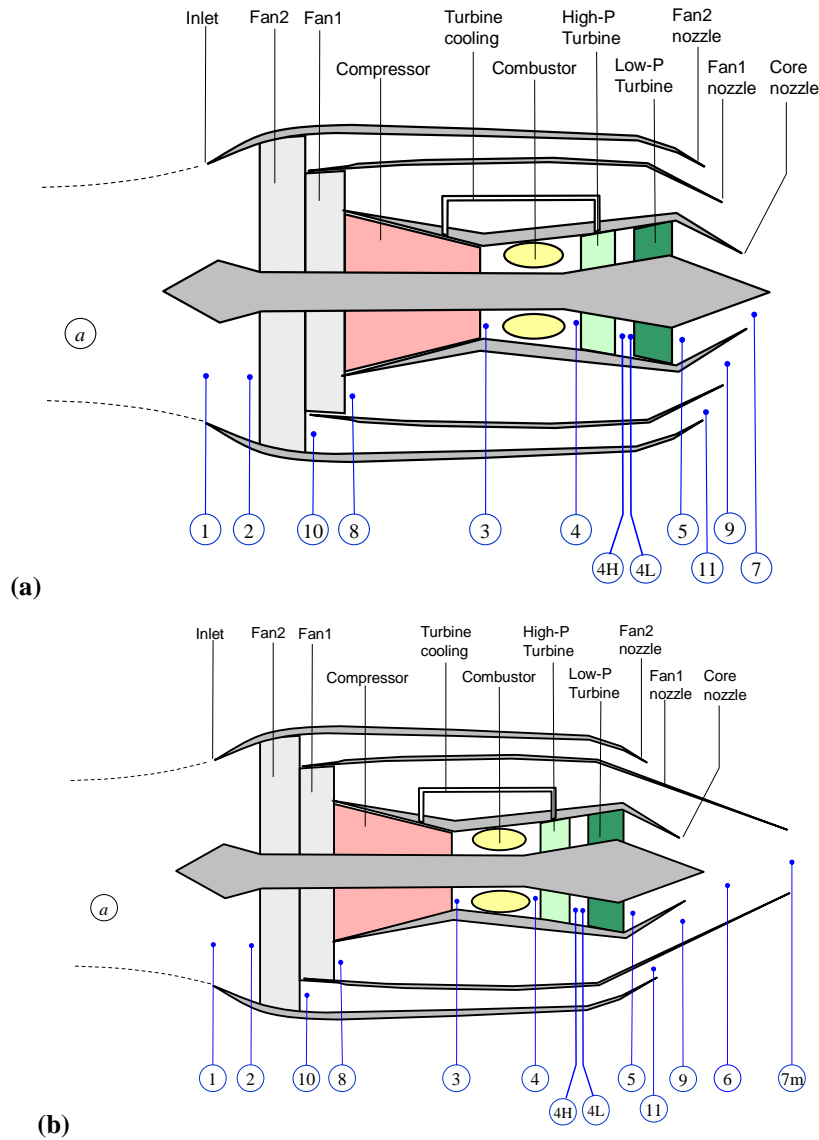


**Fig. 13: Thermodynamic models for three-stream turbofans. (a) Unmixed; (b) mixed primary and secondary streams.**

The thermodynamic cycle analysis considered a supersonic twin-engine aircraft with maximum takeoff weight of 540 kN (120,000 lb). The assumed lift-to-drag ratio is 5 at takeoff and 10 at supersonic cruise. The cruise Mach number is 1.4 at 16000 m altitude, and the takeoff Mach number is 0.3. The engine is sized for cruise, and the same diameter is used for the takeoff performance. 15% of the compressor air is used for turbine cooling, 1% of the compressor air is bled to systems outside the engine, and 1.5% of the turbine work drives auxiliary systems. Total pressure loss due to turbine cooling is estimated at 0.07 times

the mass fraction of cooling air. For the mixed-flow design, the primary and fan streams mix at constant pressure, constant total enthalpy, and Mach number 0.7 before expanding to ambient pressure. Further details on the basic analysis tools, component efficiencies, and gas constants can be found in Ref. [25].

The noise reduction scheme underpinning this project requires a significant mass flow rate (bypass ratio) of the tertiary stream. On the other hand, the selection of the tertiary bypass ratio,  $BPR_t$ , under the constraints outlined above, should be such as to ensure efficient thermodynamic operation at supersonic cruise. The first task in the cycle analysis was to examine the relation between the thrust specific fuel consumption, TSFC, against  $BPR_t$  and tertiary fan pressure ratio  $FPR_t$  (which is set equal to the secondary fan pressure ratio given that the fan is single-stage). The total bypass ratio was constrained to the value of 3.5. The resulting TSFC map for the primary and secondary streams being fully mixed (Fig. 12c) is depicted in Fig. 14. As expected, the TSFC is minimized when  $BPR_t=0$ , that is, when the entire exhaust flow is uniformly mixed. On the other hand, the design point  $BPR_t=1.0$ ,  $FPR_t = 1.82$  yields a TSFC of  $0.957 \text{ hr}^{-1}$  that is only slightly larger than the value  $0.950 \text{ hr}^{-1}$  at  $BPR_t=0$ . This set point was selected for the nozzle design. It is consistent with the bypass ratio guidance in Ref. [26].

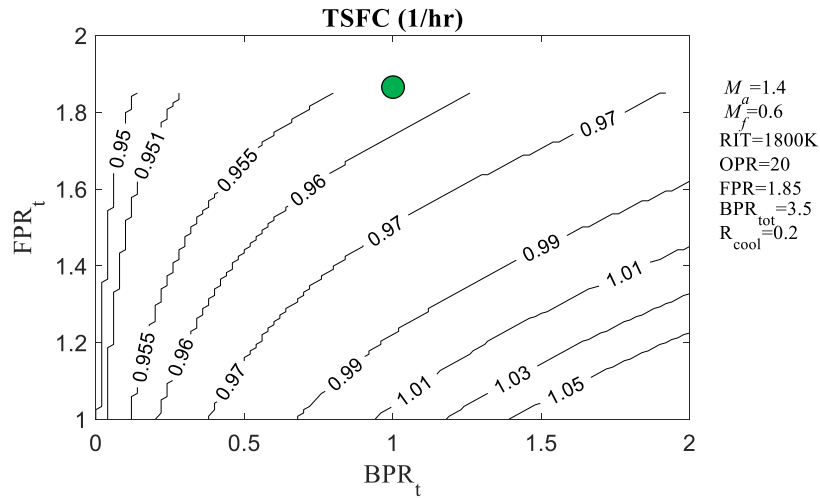


**Fig. 14** Contours of thrust specific fuel consumption at Mach 1.4 cruise versus tertiary bypass ratio ( $BPR_t$ ) and tertiary fan pressure ratio ( $FPR_t$ ). Total bypass ratio is preserved at 3.5. Symbol indicates suggested operating point.

The corresponding takeoff static conditions are depicted in Table 3.  $U$  and  $M$  are the exit velocity and Mach number, respectively. The unmixed primary and secondary conditions relate to perfect expansion to ambient pressure. In the present design the primary stream exhausts internally, in a high-pressure environment. Its local Mach number there is near 0.7.

**Table 3.** Engine cycle at takeoff condition

	NPR	BPR	$U$ (m/s)	$M$
Tertiary	1.82	1.0	338	0.967
Secondary (unmixed)	1.82	2.5	338	0.967
Primary (unmixed)	2.28	-	682	1.173
Fully-mixed primary+secondary	1.89	-	443	1.010

### C. Baseline Nozzle Design

With the nozzle areas and exhaust conditions firm up, the nozzle design went through several iterations that started with the baseline separate-flow, three-stream nozzle used in Ref. 21, named AXI04U. This nozzle features an enlarged external plug that offers some acoustic benefit but could inflict weight penalties in a realistic application. Nozzle AXI04U was then converted such that the primary and secondary streams mix internally, and the exit areas were adjusted to the conditions of Table 3. The originally external plug was reduced in sized and moved inside the common nozzle. After several iterations in which the geometry of the ducts was fine-tuned, the final design for the baseline nozzle was frozen. The design is labeled MAXI01 and its radial coordinates are plotted in Fig. 15. The diameter of the tertiary duct at the exit is  $D_t = 31.0$  mm and the diameter of the common nozzle at the exit is  $D_c = 26.6$  mm. A CAD drawing of the nozzle, used for fabrication of the article, is depicted in Fig. 16a. A photograph of the nozzle can be seen in Fig. 16b.

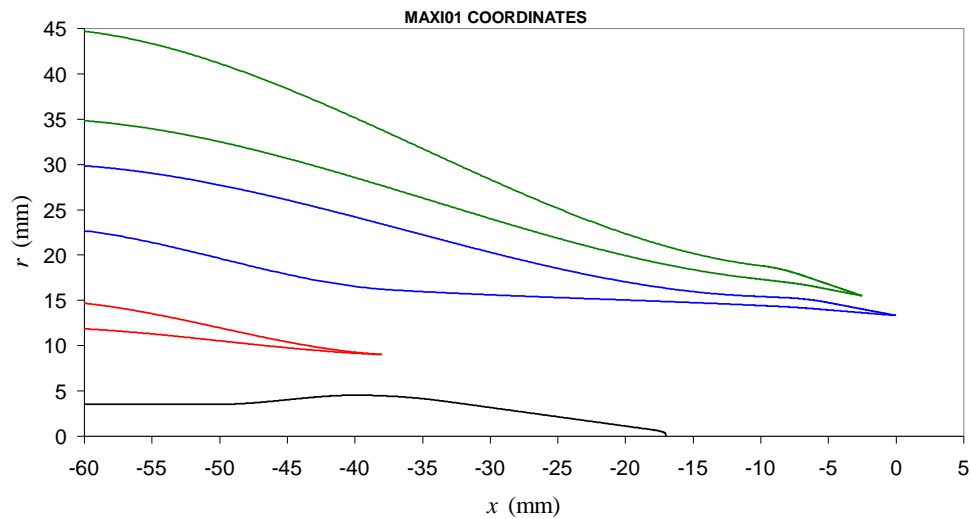


**Fig. 15** Radial coordinates of three-stream baseline (axisymmetric) nozzle MAXI01 featuring internal mixing of the primary and secondary streams.

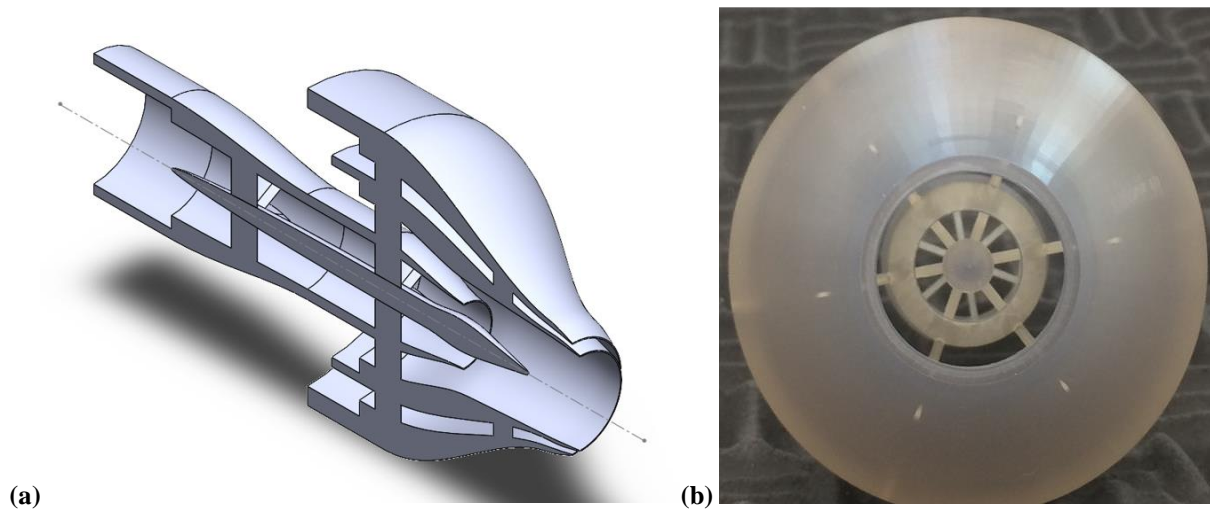


**Fig. 16** CAD view (a) and photo (b) of baseline nozzle MAXI01.

## V. Optimization Methodology

### A. Parameterization of Nozzle Reshaping

Nozzle reshaping entailed only the azimuthal distribution of the tertiary annulus width. This was not a scheme aimed at obtaining maximum noise reduction. Rather, it was an approach to optimize a well-defined geometrical feature of the nozzle. The tertiary-annulus width is denoted  $w(\phi)$ , where  $\phi$  is the azimuthal angle with respect to the downward direction ( $\phi \in [-\pi, \pi]$ ). Denoting  $w_0$  the annulus of the baseline (axisymmetric) configuration, the distribution  $w(\phi)/w_0$  is parameterized via the superposition of “bump” functions  $b$  centered at angles  $\phi_i$  and having azimuthal width  $\Phi$ :

$$\frac{w}{w_0} = 1 + \sum_{i=-N}^N S_i b(\phi - \phi_i, \Phi) \quad (22)$$

where  $S_i$  are the shape coefficients. The total number of bumps is  $2N+1$ . The bumps are arranged symmetrically around the plane of symmetry of the nozzle, that is,  $S_{-i} = S_i$  and  $\phi_{-i} = -\phi_i$ . By definition,  $\phi_0 = 0$ . The bump function is selected to be the *diminished Gaussian*

$$b(\phi, \Phi) = e^{-(\phi/\Phi)^2} - \frac{\Phi}{2\sqrt{\pi}} \quad (23)$$

which satisfies

$$\int_{-\pi}^{\pi} b(\phi, \Phi) d\phi \approx 0, \quad \Phi \leq 1.2\pi \quad (24)$$

For a thin annulus, Eq. 24 ensures that the annulus area remains constant (to within a fraction of a percent) and equal to the tertiary exit area of the baseline nozzle. An arbitrary number of bumps can be used, and the area remains virtually constant. Figure 17 illustrates the effect of a single bump on the geometry of the tertiary annulus.

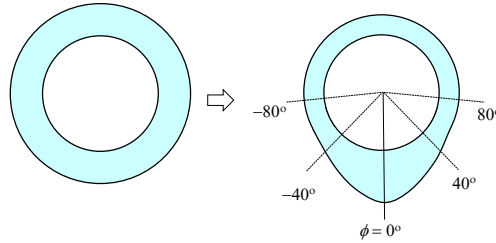


**Fig. 17 Illustration of the distortion of the tertiary annulus using a single bump centered at  $\phi=0^\circ$ . The design process combined bumps at  $\phi=0^\circ, \pm 40^\circ$  and  $\pm 80^\circ$ .**

The focus here was placed on improving  $\Delta EPNL_{TO+SL}$  by a parametric coverage of tertiary-annulus distortions while maintaining a constant overall eccentricity (as quantified below) at a fairly high level.

### B. Design of Experiments Approach

A central goal of the research is construction of a response surface of an objective function  $y$  in terms of the nozzle shape parameter vector  $S_i$  given a selection of bump azimuthal angles  $\phi_i$ . The response surface would guide the design to an optimal  $S_i$ , which would then be investigated experimentally. We seek definition of a response surface with a minimum number of RANS solutions. We follow some basic principles of factorial design of experiments, with modifications to address the unique features and constraints of the nozzle design. The approach is inspired by earlier works that used Design of Experiments (DOE) to maximize noise reduction using chevrons and vane deflectors [13,14].

We select a design with 5 bumps ( $N=2$ ) with  $\phi_0 = 0^\circ$ ,  $\phi_1 = 40^\circ$ , and  $\phi_2 = 80^\circ$ . The parameter vector consists of three elements,  $S_0$ ,  $S_1$  and  $S_2$ , which will assume three levels. Although initially this looks like a  $3^3$  factorial design, constraints will reduce it to a  $3^2$  design. The azimuthal scale for all the bumps is selected to be  $\Phi = 40^\circ$ . We impose the constraint

$$\sum_{i=-N}^N S_i = S_{tot} \quad (25)$$

where  $S_{tot}$  is a measure of the total eccentricity of the annulus and is treated here as a preserved quantity. For the 5-bump design, this becomes

$$S_0 + 2(S_1 + S_2) = S_{tot} \quad (26)$$

Further, we require that all the bumps be non-negative, that is,

$$S_0 \geq 0, S_1 \geq 0, S_2 \geq 0 \quad (27)$$

For bump placements and scales that allow all the Gaussian tails to essentially vanish at  $\phi = 180^\circ$  (top of the nozzle),  $S_{tot}$  is directly connected to the minimum annulus width at the top of the nozzle,  $w_{top}$ , via the relation

$$S_{tot} = \left(1 - \frac{w_{top}}{w_0}\right) \frac{2\sqrt{\pi}}{\Phi} \quad (28)$$

From a practical standpoint, it is desired to maintain this minimum width at the fabrication tolerance so that the annulus remains open. Based on experience with the fabrication facility, this tolerance is  $w_{top} = 0.65$  mm. For the tertiary-annulus dimensions of the MAXI01 nozzle (Fig. 18), the corresponding total eccentricity is  $S_{tot} = 2.832$ .

### C. Transformed and Coded Variables

The constraint of Eq. 26 reduces the number of independent variables to two, which are selected to be  $S_1$  and  $S_2$ . They are constrained by the relation

$$S_0 = S_{tot} - 2(S_1 + S_2) \geq 0 \quad (29)$$

or

$$\frac{2}{S_{tot}}(S_1 + S_2) \leq 1 \quad (30)$$

As shown in Fig. 18a, the  $(S_1, S_2)$  parameter space is triangular, bounded on the left by  $S_1=0$ , on the bottom by  $S_2=0$ , and on the top by the line  $\frac{2}{S_{tot}}(S_1 + S_2) = 1$ . This prevents a regular design of experiments and complicates the optimization. This limitation is circumvented here through variable transformations. First, we define

$$q_1 = \sqrt{\frac{2S_1}{S_{tot}}}, q_2 = \sqrt{\frac{2S_2}{S_{tot}}} \quad (31)$$

Now Eq. 30 takes the form

$$q_1^2 + q_2^2 \leq 1 \quad (32)$$

The  $(q_1, q_2)$  space is a quarter-circle with radius 1, as shown in Fig. 18b, which motivates the formulation

$$q_1 = R \cos \psi, q_2 = R \sin \psi \quad (33)$$

with  $R \in [0, 1]$  and  $\psi \in [0, \pi/2]$ .  $R=0$  represents a design with  $S_0=S_{tot}$ , concentrating all the eccentricity downward.  $R=1$  means that the downward bump is zero. From past experience, the  $R=0$  design is expected to be poor because it will offer very little if any sideline noise reduction. So, it is advisable to start the exploration of  $R$  at a higher level, in the interval  $R \in [R^*, 1]$ , where  $0 < R^* < 1$ .

To conform with the requirements of constructing a response surface,  $R$  and  $\psi$  are expressed in terms of coded variables  $x_1$  and  $x_2$ , respectively, both of which are in the range  $[-1, 1]$ :

$$R = R^* + \frac{1}{2}(1 - R^*)(x_1 + 1) \quad (34)$$

$$\psi = \frac{\pi}{4}(x_2 + 1) \quad (35)$$

The resulting design space is shown in Fig. 18c. Combining Eqs. 31, 33, 34, and 35, the relations between the natural and coded variables are:

$$S_1 = \frac{S_{tot}}{2} \left\{ \left[ R^* + \frac{1}{2}(1 - R^*)(x_1 + 1) \right] \cos \left[ \frac{\pi}{4}(x_2 + 1) \right] \right\}^2, \quad -1 \leq x_1 \leq 1, \quad -1 \leq x_2 \leq 1 \quad (36)$$

$$S_2 = \frac{S_{tot}}{2} \left\{ \left[ R^* + \frac{1}{2}(1 - R^*)(x_1 + 1) \right] \sin \left[ \frac{\pi}{4}(x_2 + 1) \right] \right\}^2, \quad -1 \leq x_1 \leq 1, \quad -1 \leq x_2 \leq 1 \quad (37)$$

$$S_0 = S_{tot} - 2(S_1 + S_2) \quad (38)$$

#### D. Response Surface Methodology

The response surface is formulated in the coded variable vector  $\mathbf{x}=(x_1, x_2)$  in terms of radial basis functions  $G(r)$  that depend on the distance  $r$  between  $\mathbf{x}$  and each data point  $\mathbf{x}_i$ . The development below is based on McDonald *et al.* [16]. For  $M$  runs, the response surface is approximated by

$$y = \sum_{i=1}^M \beta_i G(|\mathbf{x} - \mathbf{x}_i|) \quad (39)$$

where  $\beta_i$  are the radial basis coefficients for each point  $\mathbf{x}_i$ . Evaluation of Eq. 39 at the data points gives

$$y_j = \sum_{i=1}^M \beta_i G(|\mathbf{x}_j - \mathbf{x}_i|), \quad j = 1, \dots, M \quad (40)$$

On defining  $\mathbf{y} = y_j$ ,  $\boldsymbol{\beta} = \beta_i$  and  $\mathbf{A} = G(|\mathbf{x}_j - \mathbf{x}_i|)$ , Eq. 40 can be written in matrix form as.

$$\mathbf{y} = \mathbf{A}\boldsymbol{\beta} \quad (41)$$

For a certain class of radial basis functions, and with the coded parameter range as defined in Eqs. 36 and 37, the  $M \times M$  matrix  $\mathbf{A}$  is guaranteed to be non-singular. The coefficients are then obtained from

$$\boldsymbol{\beta} = \mathbf{A}^{-1}\mathbf{y} \quad (42)$$

Among the radial basis functions that guarantee a non-singular  $\mathbf{A}$ , the Gaussian

$$G(r) = e^{-cr^2} \quad (43)$$

is selected here. The constant  $c$  is user-defined and here took the value  $c=1$ .

#### E. Design Space

The design space in terms of the coded variables is depicted in Fig. 18c. Each coded variable takes the values  $-1, 0$ , and  $1$ , resulting in 9 runs. The lower bound for  $R, R^*$ , in Eq. 34 is selected such that  $S_0=S_1=S_2$  at the central point  $(0,0)$ . For the dimensions of the current annulus, the resulting value is  $R^*=0.789$ . Table 4 lists the coded and natural variables for the design matrix. Figure 19 plots the tertiary-annulus geometry for the cases listed in Table 4. The axisymmetric nozzle (MAXI01) is included for reference.

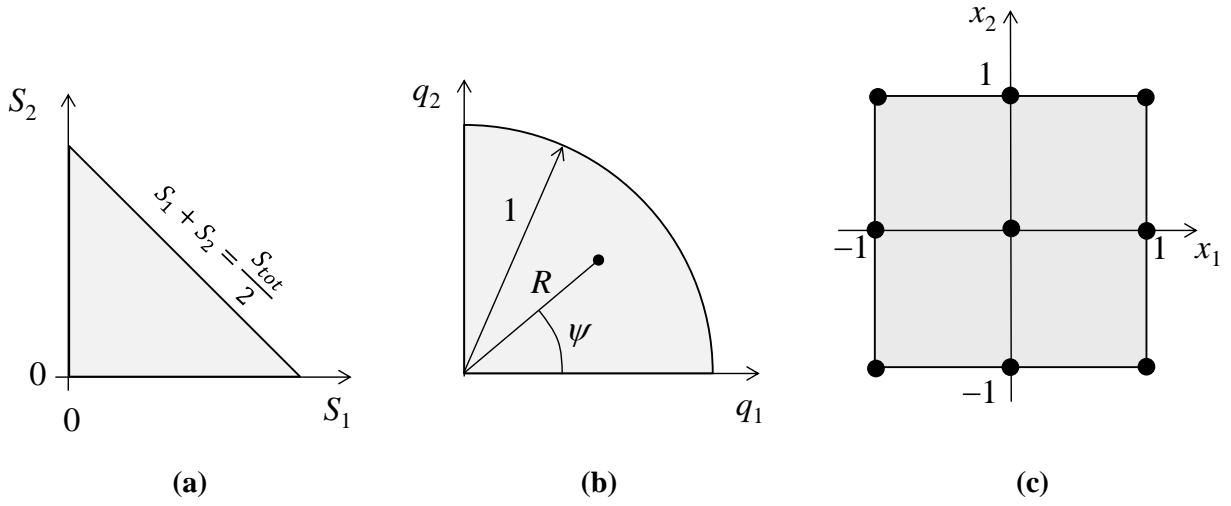
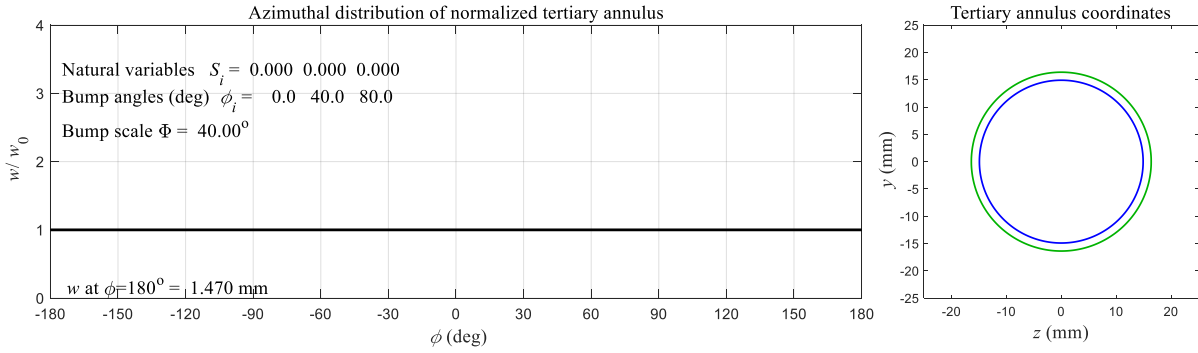


Fig. 18 Design space in terms of: (a) natural variables; (b) transformed variables; (c) coded variables.

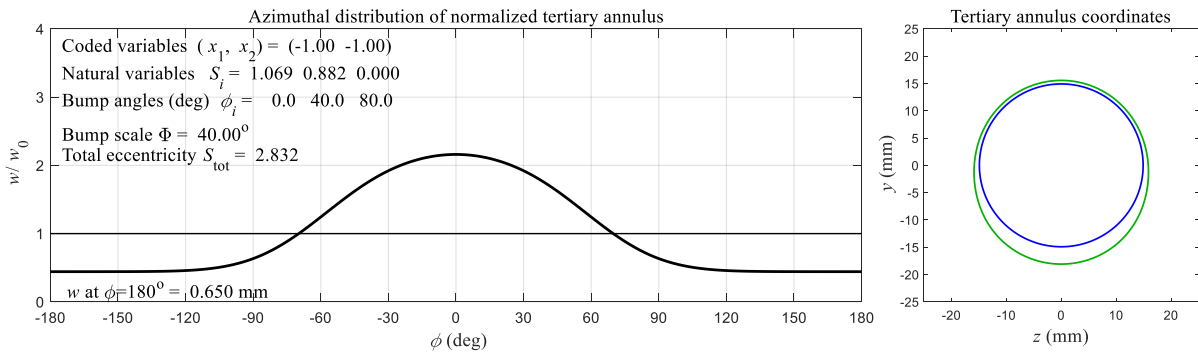
Table 4 Design of Experiments Matrix

Nozzle	Coded Variables		Natural Variables		
	$x_1$	$x_2$	$S_0$	$S_1$	$S_2$
MECC01	-1.0	-1.0	1.068	0.881	0.000
MECC02	-1.0	0.0	1.068	0.440	0.440
MECC03	-1.0	1.0	1.068	0.000	0.881
MECC04	0.0	-1.0	0.566	1.132	0.000
MECC05	0.0	0.0	0.566	0.566	0.566
MECC06	0.0	1.0	0.566	0.000	1.132
MECC07	1.0	-1.0	0.000	1.415	0.000
MECC08	1.0	0.0	0.000	0.708	0.708
MECC09	1.0	1.0	0.000	0.000	1.415

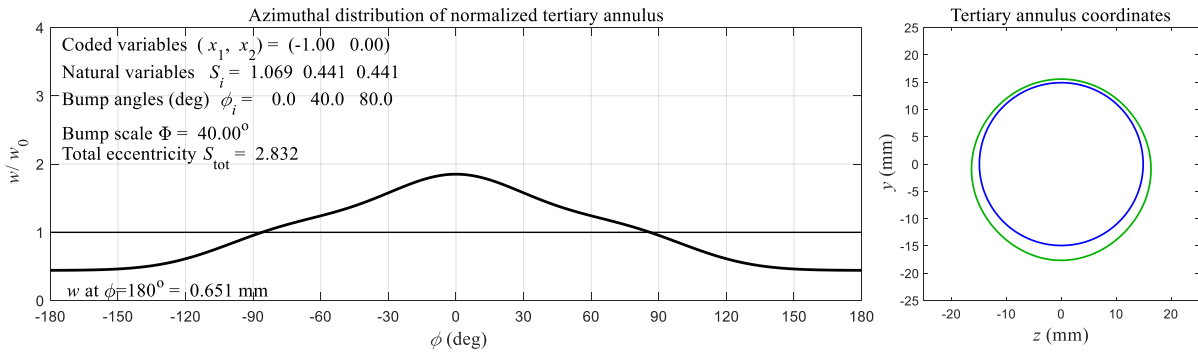
# MAXI01



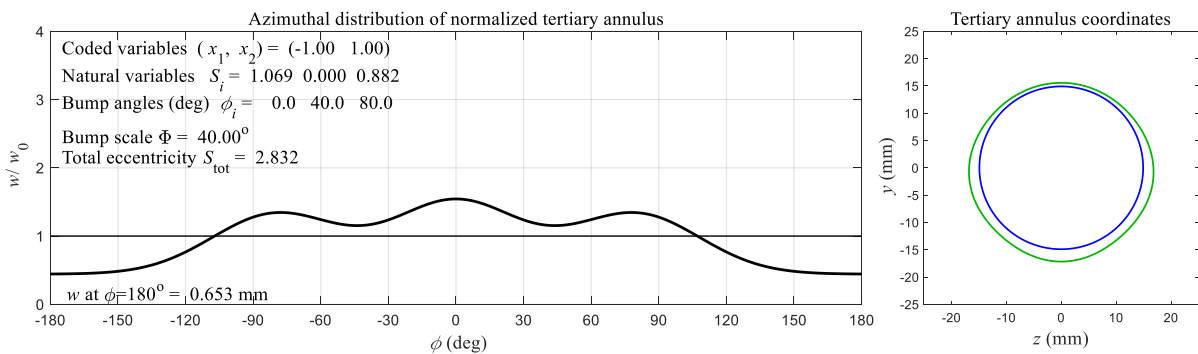
# MECC01



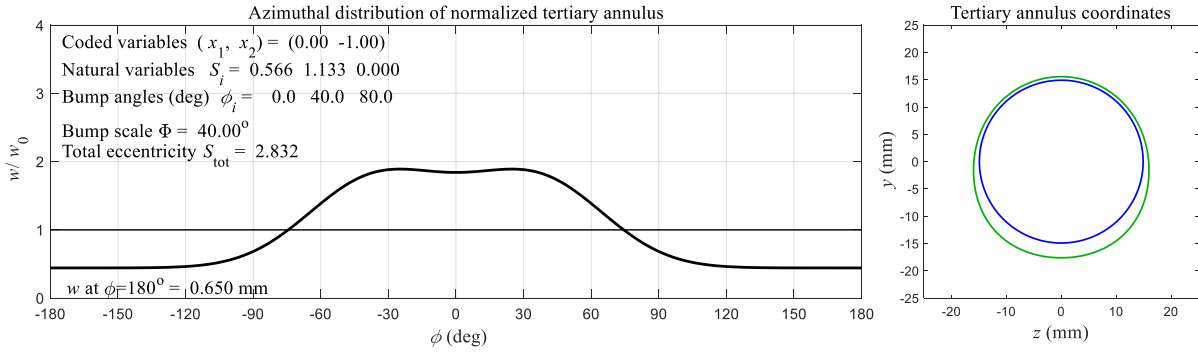
# MECC02



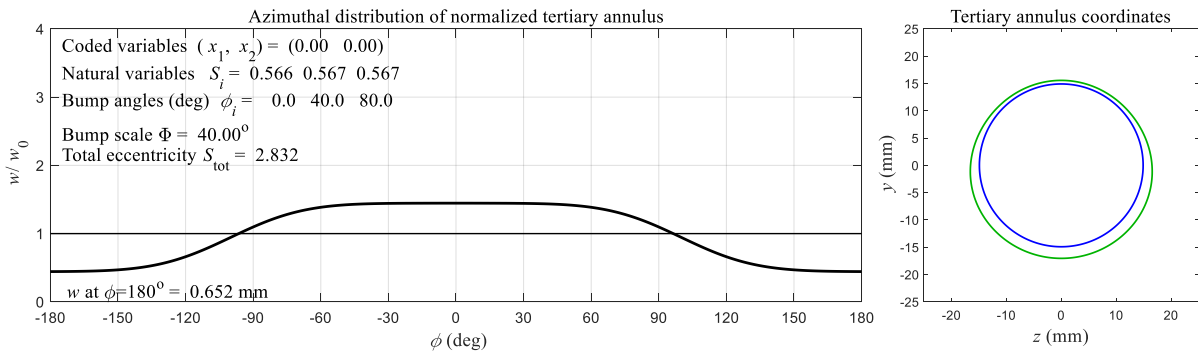
# MECC03



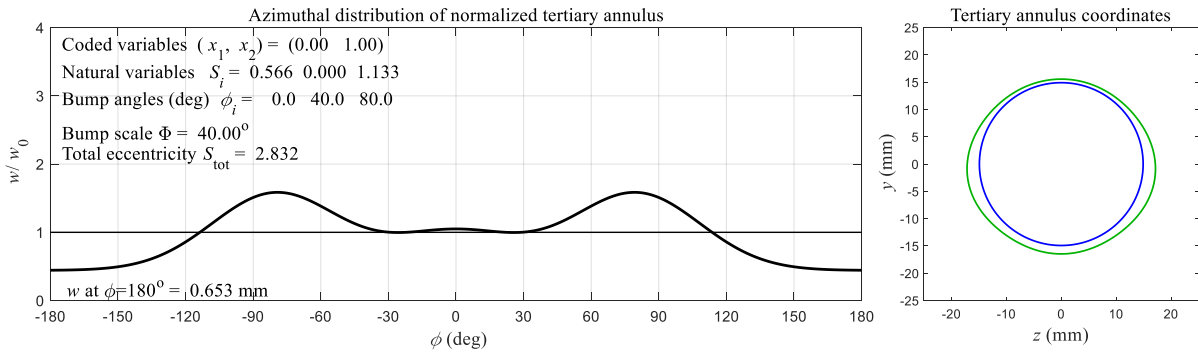
### MECC04



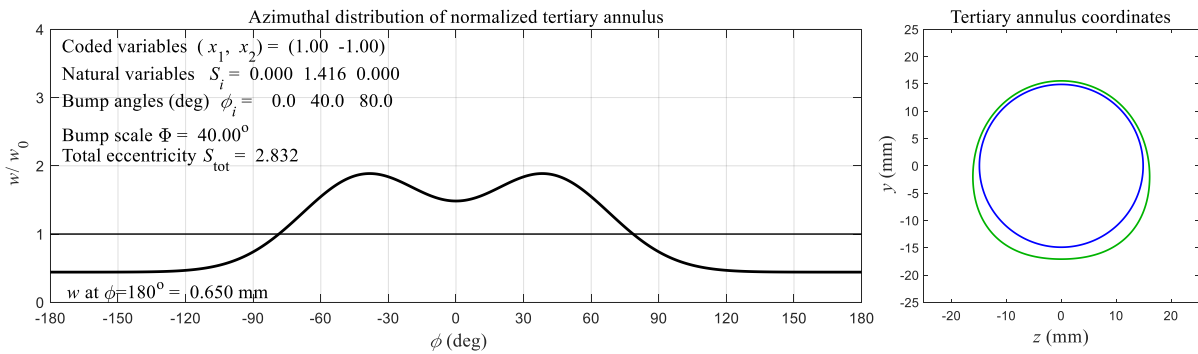
### MECC05



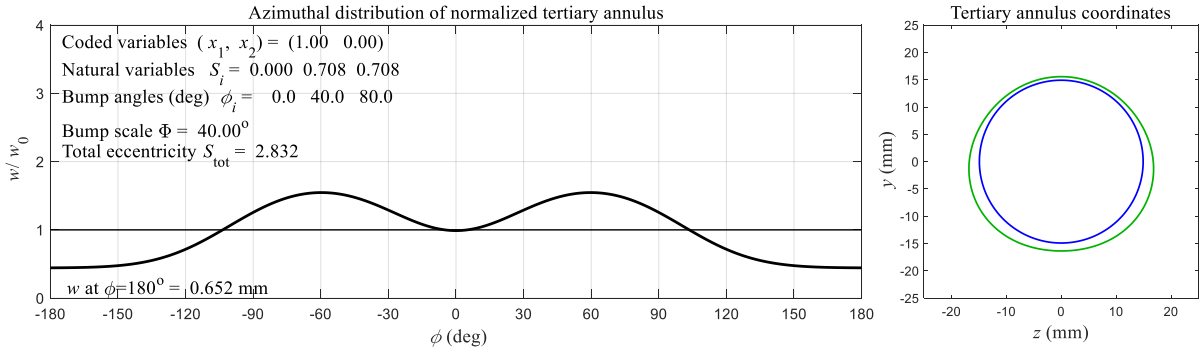
### MECC06



### MECC07



MECC08



MECC09

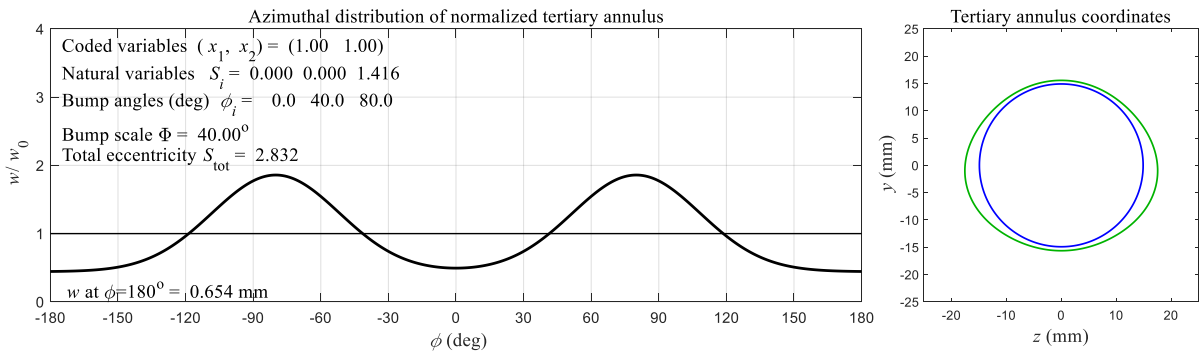


Fig. 19 Tertiary-annulus geometry of the baseline nozzle (MAXI01) and the cases of Table 4.

## VI. RANS Simulations

### A. Role

Reynolds-Averaged Navier Stokes (RANS) simulations generated statistics in the jet plume that were used in the modeling of jet noise and its reduction. In addition, they provided measures of aerodynamic performance (thrust loss, mass-flow-rate loss) that helped determine the practical feasibility of nozzle designs.

### B. Thermodynamic Conditions for Unmixed Cycle

The detailed thermodynamic conditions used in the RANS simulations of the unmixed cycle (corresponding to Table 3) are provide in Table 5. The cycle is labeled D8840 following an extension of NASA's terminology (D for  $NPR_p = 2.3$ ; 8 for  $NPR_s = 1.82$ ; 8 for  $NPR_t = 1.82$ ; 4 for  $TTR_p = 3.7$ ; 0 for zero forward velocity). The ambient conditions are 101325 Pa and 290°K

Table 5. Cycle D8840 Thermodynamic Conditions

Stream	Total pressure (Pa)	Total temperature (°K)	Fully expanded Mach number
Primary	237101	1073	1.173
Secondary	184412	363	0.967
Tertiary	184412	363	0.967

### C. Interior Flow Field for Baseline Nozzle

Examination of the internal flow field was important for verifying the flow quality of the nozzle design. Specifically, we looked for instances of flow separation that would adversely impact the fluid dynamics and noise. The flow field was found to be without any problematic aspects. Figure 20 presents isocontours of the mean axial velocity in the interior of the nozzle and initial few diameters of the plume. There is no evidence of flow separation in the nozzle ducts. Mixing between the primary and secondary streams is slow, as expected, and the exit velocity profile represents an essentially unmixed configuration. The wake of the plug is seen to persist past the nozzle exit.

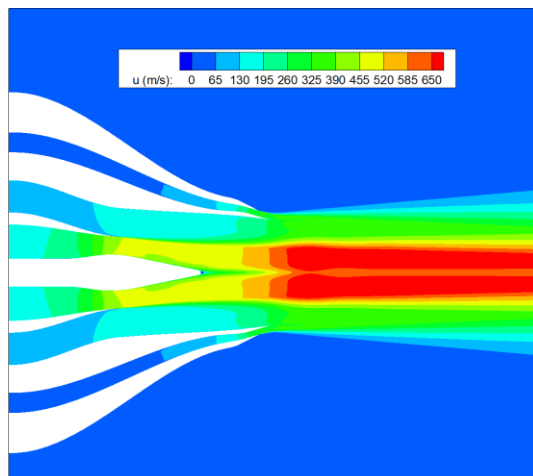
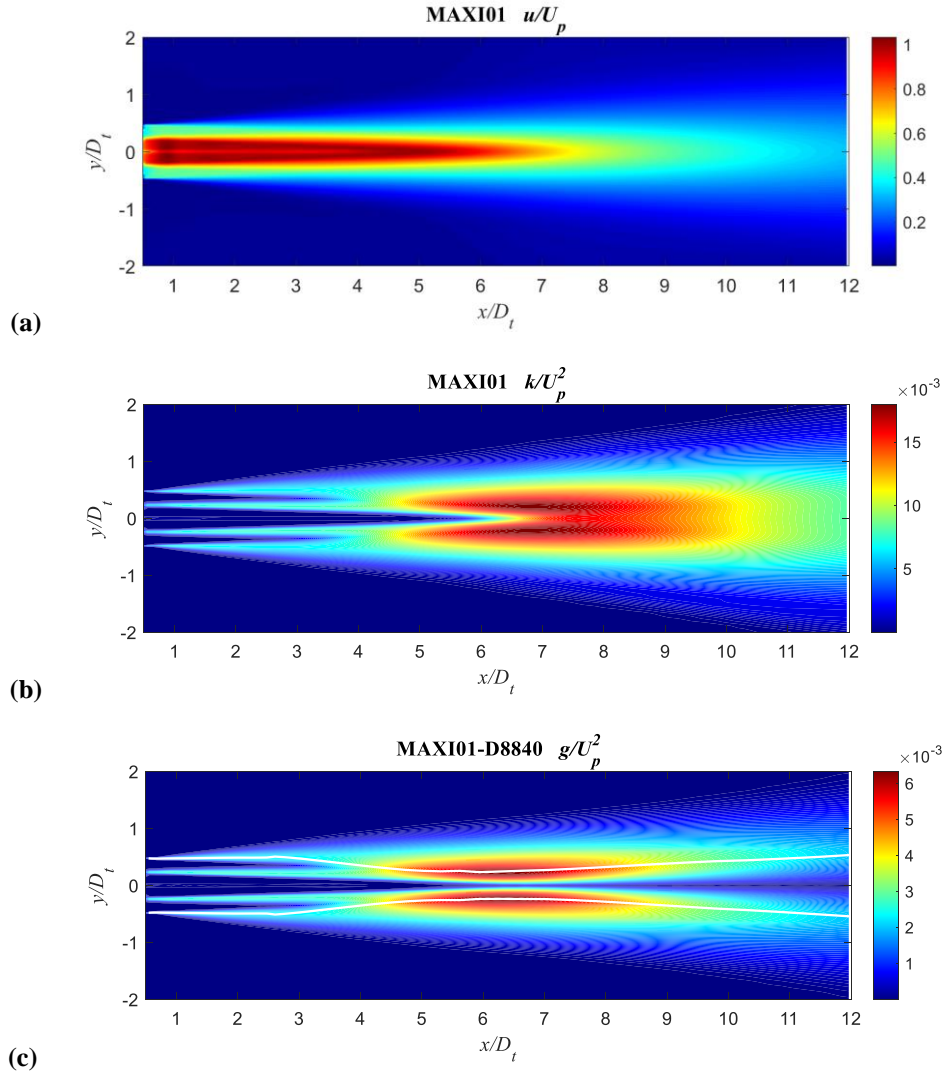


Fig. 20 Isocontours of mean axial velocity on the plane of symmetry inside and immediately outside nozzle MAXI01 at cycle D8840.

#### D. Exterior Flow Field for Baseline Nozzle

We examine distributions of time-averaged quantities on the  $x$ - $y$  symmetry plane. The tertiary exit diameter  $D_t$  is used to normalize the axes. Figure 21 depicts isocontours of mean axial velocity  $\bar{u}$ , turbulent kinetic energy  $k$ , and Reynolds stress  $g$ . All are appropriately normalized using the ideally-expanded primary exit velocity  $U_p$  as velocity scale. The plot of normalized mean axial velocity  $\bar{u}/U_p$ , Fig. 21a, indicates that the maximum local velocity starts declining past  $x/D_t=6$ , thus marking the end of the primary potential core. The wake of the nozzle plug persists up to about  $x/D_t = 4$ .



**Fig. 21 Isocontours on the symmetry plane in the plume of jet MAXI01 at cycle D8840: (a) mean axial velocity; (b) turbulent kinetic energy; (c) Reynolds stress, with white line indicating the outer surface of peak stress (OSPS).**

The plot of normalized turbulent kinetic energy  $k/U_p^2$ , seen in Fig. 21b, shows the primary potential core ending at  $x/D_t = 6$  (consistent with the observation of the mean axial velocity field) and the secondary/tertiary potential core ending at  $x/D_t = 3.8$  (because the secondary and tertiary streams have equal exit velocities, they form a common potential core). The turbulent kinetic energy peaks at the value  $k/U_p^2 =$

0.018 near  $x/D_t=7$ . This peak level is similar to those seen in previous multi-stream jets [5]. Past  $x/D_t=9$ , the turbulent kinetic energy forms a jet-like profile.

Figure 21c presents the distribution of normalized Reynolds stress  $g/U_p^2$ . Like the plot of turbulent kinetic energy, it shows the primary and secondary/tertiary potential cores ending at  $x/D_t=6$  and 3.8, respectively. The peak value of  $g/U_p^2=0.0065$  occurs at  $x/D_t=6.5$ , slightly upstream of the peak of turbulent kinetic energy. This peak value is similar to those computed in earlier three-stream jets [5]. In contrast with the far-field behavior of turbulent kinetic energy, the Reynolds stress peaks off the jet axis near the locus of maximum mean velocity gradient. The white line in Fig. 21c tracks the location of the outer surface of peak Reynolds stress (OSPS). The transition of the OSPS from the outer to the inner shear layer is evident near  $x/D_t=3.5$ . Downstream of this collapse the OSPS converges to a “throat” near the location of peak Reynolds stress, then diverges as the jet spreads.

A three-dimensional representation of the OSPS is shown in Fig. 22. The features just mentioned are evident. Isocontours of the convective Mach number  $M_c$  (modeled as the mean axial velocity on the OSPS divided by the ambient speed of sound) are superimposed on the surface.  $M_c$  starts from the low value of 0.65 and maintains this value up to  $x/D_t=3.5$ , before the collapse of the OSPS. Downstream of the collapse  $M_c$  reaches a peak value of about 1.2 which persists up to  $x/D_t=6.5$ . The supersonic value of  $M_c$  over this region indicates generation of strong Mach wave radiation. Reducing  $M_c$  on the underside of the jet is a key driver for the nozzle redesign effort.

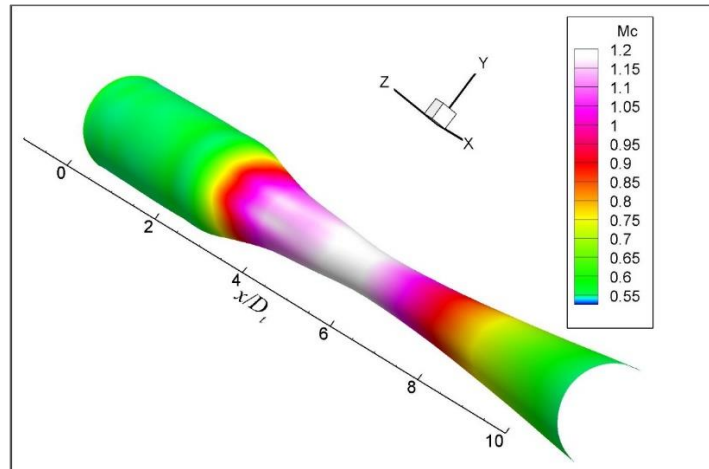


**Fig. 22 Outer Surface of Peak Reynolds Stress (OSPS) for jet MAXI01 at cycle D8840. Contours indicate level of convective Mach number  $M_c$ .**

### E. OSPS for All the Jets

The simulations comprised the three-stream axisymmetric nozzle (MAXI01) and its nine asymmetric variants (MECC01 through MECC09). Thus, a total of 10 RANS simulations were conducted. The RANS data were processed to yield all the quantities of interest for the differential acoustic analogy model. The most relevant result is the outer surface of peak stress (OSPS) and the distributions of convective Mach number, mean density, turbulent kinetic energy, and Reynolds stress on it [15]. Figure 23 plots the OSPS for all the jets. The sensitivity of the deformation of the mean flow on the nozzle initial condition is evident.

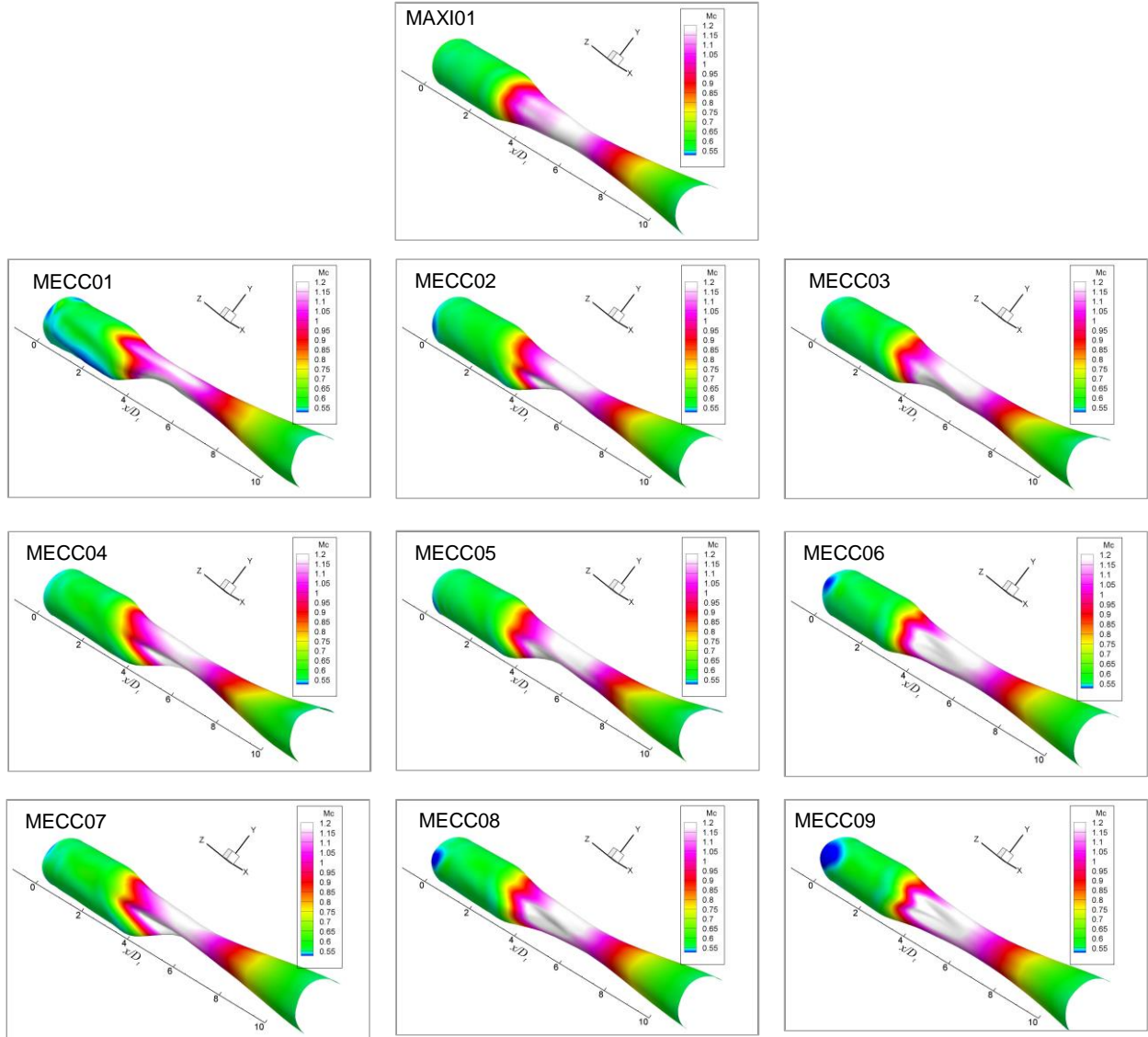


**Fig. 23 Outer surface of peak Reynolds stress (OSPS) for all the jets at unmixed cycle D8840. Isocontours of convective Mach are plotted on the surfaces.**

## VII. Optimization

### A. Summary of Prediction and Optimization Methodology

With the parameter vector  $\mathbf{V}$  determined and the RANS simulations of the DOE cases completed, the optimization can be completed. The process is illustrated in Fig. 24. The differential SPL,  $\Delta\text{SPL}$ , for each DOE case is calculated according to the model described in Section III. The  $\Delta\text{SPL}$  is added to the baseline spectrum to obtain the synthetic SPL spectra for all the DOE cases. Each SPL spectrum is then “flown” according to a prescribed aircraft trajectory to estimate the EPNL. An acoustic response surface is then constructed.

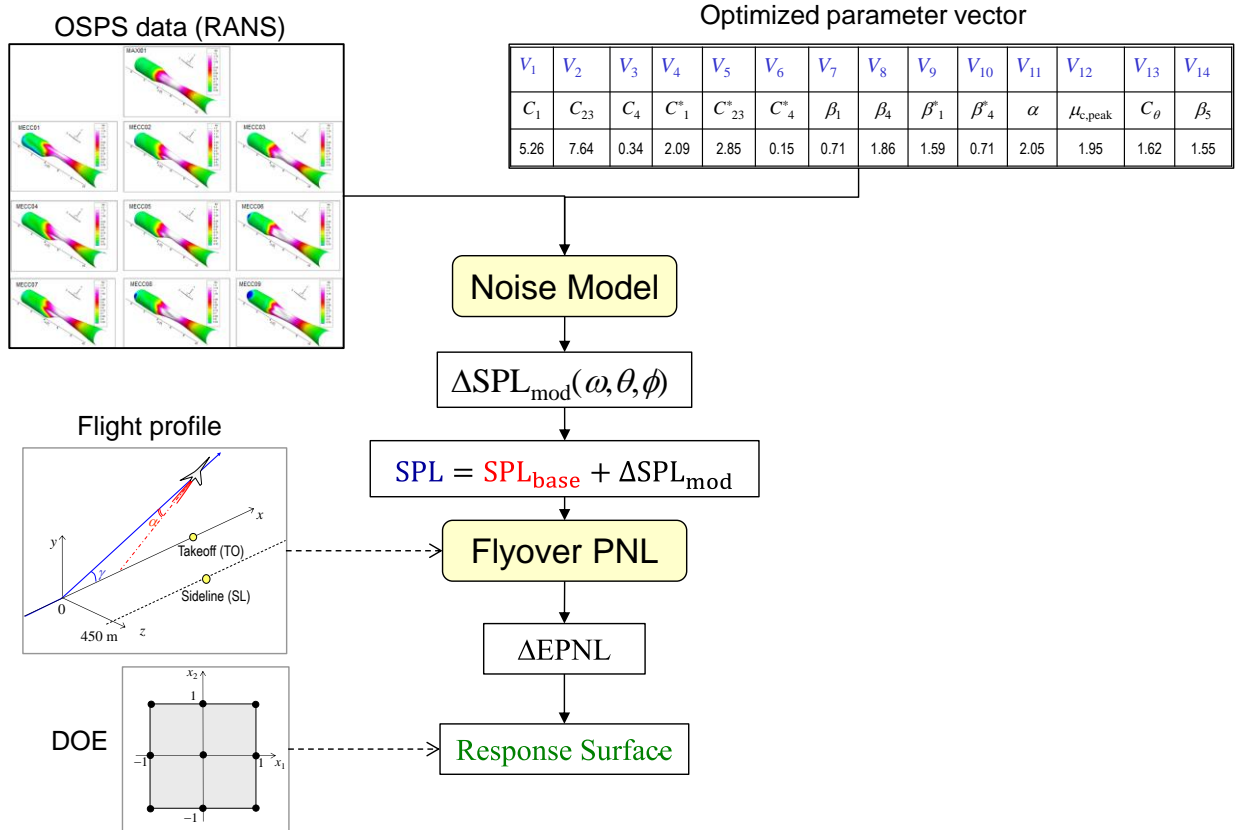


Fig. 24 Summary of prediction and optimization process.

### B. SPL Spectrum for Baseline Jet

Carefully-set helium-air mixtures were used to match the Mach numbers and velocities for cycle D8840. The SPL spectra for jet MAXI01 at cycle D8840 are plotted in Fig. 25 for various polar angles. The peak emission is near  $\theta = 35^\circ$ . A small spectral bump at high angles indicates broadband shock associated noise, which is expected given the slightly underexpanded primary stream.

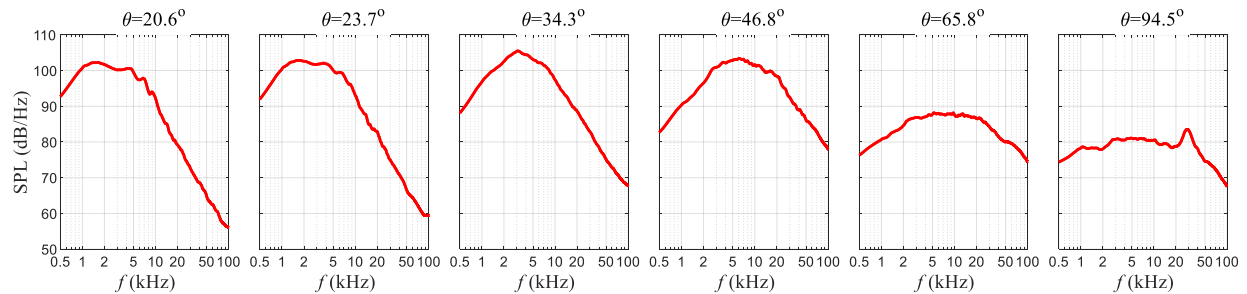


Fig. 25 Experimental SPL spectra of baseline nozzle MAXI01 at cycle D8840.

### C. Acoustic Response Surface

For the acoustic results, the response  $y$  of the DOE process is defined as the “cumulative” reduction in EPNL at the takeoff and sideline monitors, symbolized  $\Delta\text{EPNL}_{\text{TO+SL}}$ . It is listed in Table 7. The

corresponding response surface, constructed according to Section V.D, is plotted in Fig. 26. There is an evident maximum (indicated by the green dot) at  $(x_1, x_2) = (0.3, -0.9)$ .

The location of the optimal point was fairly insensitive to moderate variations of the parameter vector and even to the baseline spectrum used to construct the synthetic SPL.

**Table 7 DOE Matrix including Acoustic Response**

Nozzle	Coded Variables		Natural Variables			Response
	$x_1$	$x_2$	$S_0$	$S_1$	$S_2$	$y = \Delta\text{EPNL}_{\text{TO+SL}}$
MECC01	-1.0	-1.0	1.068	0.881	0.000	1.54
MECC02	-1.0	0.0	1.068	0.440	0.440	3.15
MECC03	-1.0	1.0	1.068	0.000	0.881	1.35
MECC04	0.0	-1.0	0.566	1.132	0.000	3.68
MECC05	0.0	0.0	0.566	0.566	0.566	2.07
MECC06	0.0	1.0	0.566	0.000	1.132	1.05
MECC07	1.0	-1.0	0.000	1.415	0.000	3.05
MECC08	1.0	0.0	0.000	0.708	0.708	2.02
MECC09	1.0	1.0	0.000	0.000	1.415	0.67

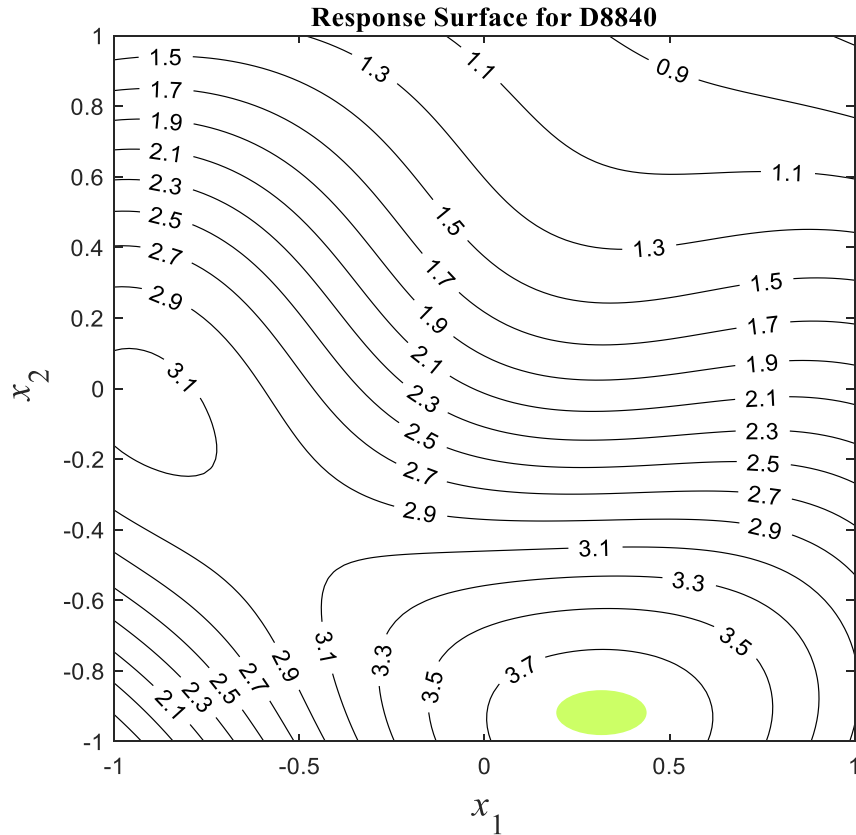


**Fig. 26 Response surface for cumulative EPNL reduction (dB) for cycle D8840.**

## D. Aerodynamic Response Surface

The RANS solutions also yield estimates of the effect of the tertiary annulus eccentricity on aerodynamic performance of the nozzle. The latter is quantified as the loss in specific thrust. The response surface for specific thrust loss is shown in Fig. 27. Because the offset scheme used was not aggressive, the thrust loss is very minor, no larger than 0.04%. Being so small, the thrust loss does not impact the evaluation of the quietest configuration. At the location of the acoustically optimal point  $(x_1, x_2) = (0.3, -0.9)$  the specific thrust loss is only 0.02%.

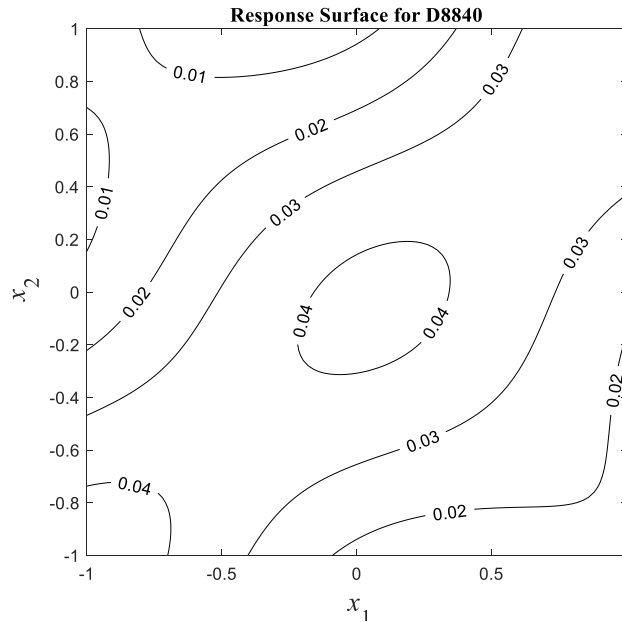
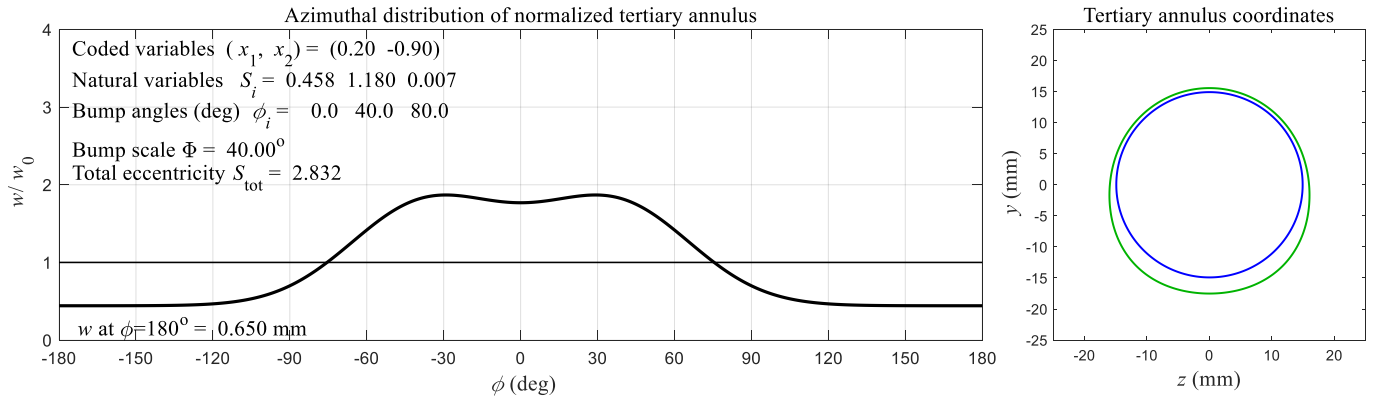


Fig. 27 Response surface for percent loss in specific thrust (cycle D8840).

## E. Optimal Nozzle Design

For practical reasons, the optimal nozzle was determined from a preliminary response surface that indicated an optimal EPNL reduction at  $(x_1, x_2) = (0.2, -0.9)$  versus  $(0.3, -0.9)$  for the final response surface. It is evident from Fig. 26 that this difference is minor.

The resulting azimuthal distribution of the tertiary annulus is plotted in Fig. 28. Figure 29 depicts a CAD drawing and photograph of the optimal nozzle, which is labeled MECC10.



**Fig. 28 Tertiary-annulus geometry of the optimal nozzle (MECC10).**

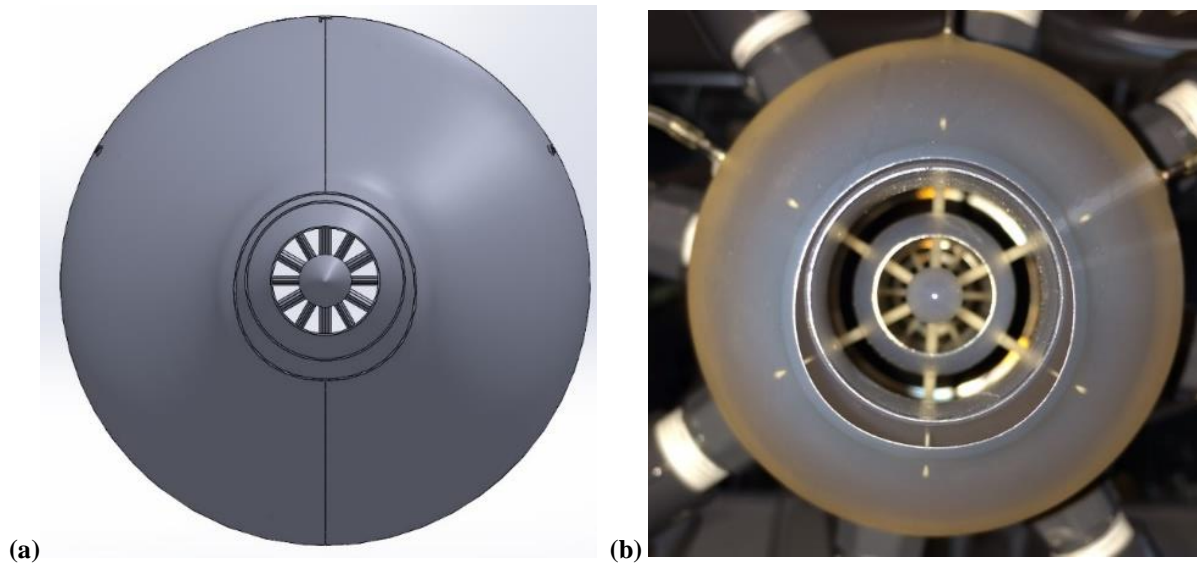


**Fig. 29 (a) CAD drawing and (b) photograph of optimal nozzle MECC10.**

### VIII. Experimental Verification

The optimal nozzle MECC10 was tested at the unmixed cycle conditions D8840. As with the testing of MAXI01, helium-air mixtures were used to match the Mach numbers and velocities of this cycle.

The experimental SPL spectra for jets MAXI01 and MECC10 are compared in Fig. 30 for various polar and azimuthal angles. Significant reductions in SPL are observed for azimuthal angles  $\phi = 0^\circ$  and  $30^\circ$ . Little or no benefit is registered for  $\phi \geq 60^\circ$ .

The corresponding histories of perceived noise level  $PNL(t)$  and the estimates of EPNL are shown in Fig. 31. The cumulative EPNL reduction is  $\Delta EPNL_{TO+SL} = 2.9$  dB versus 3.8 dB predicted by the model (Fig. 26). The breakdown in takeoff and sideline reductions is: 2.9 dB and 0.0 dB for the experiment; 2.5 dB and 1.3 dB for the model. The main reason for the discrepancy in  $\Delta EPNL_{TO+SL}$  is that the model overpredicts moderately the acoustic benefit at large azimuthal angles.

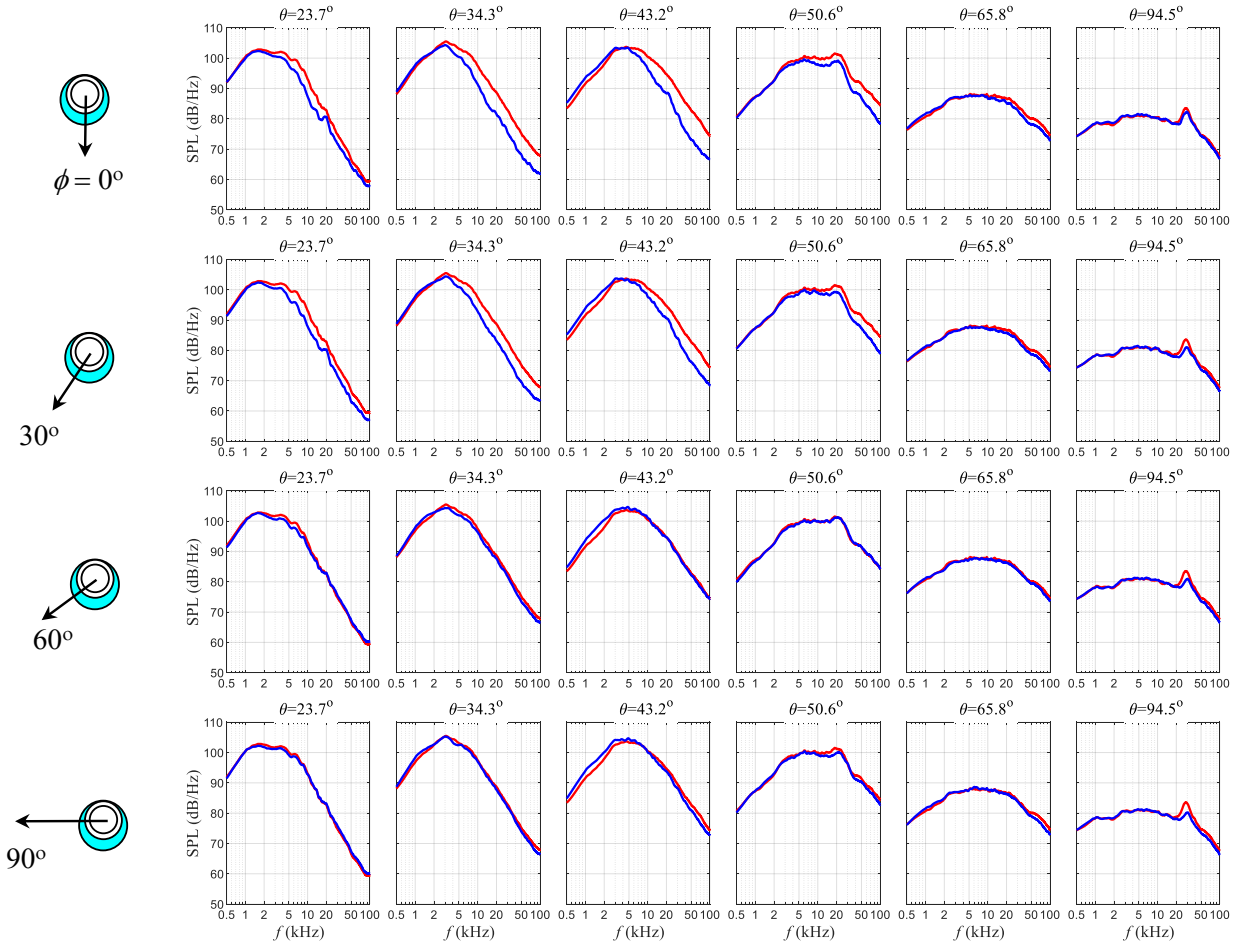


**Fig. 30 Experimental SPL spectra at various polar and azimuthal angles for jet MECC10 (blue lines) compared to baseline jet MAXI01 (red lines).**

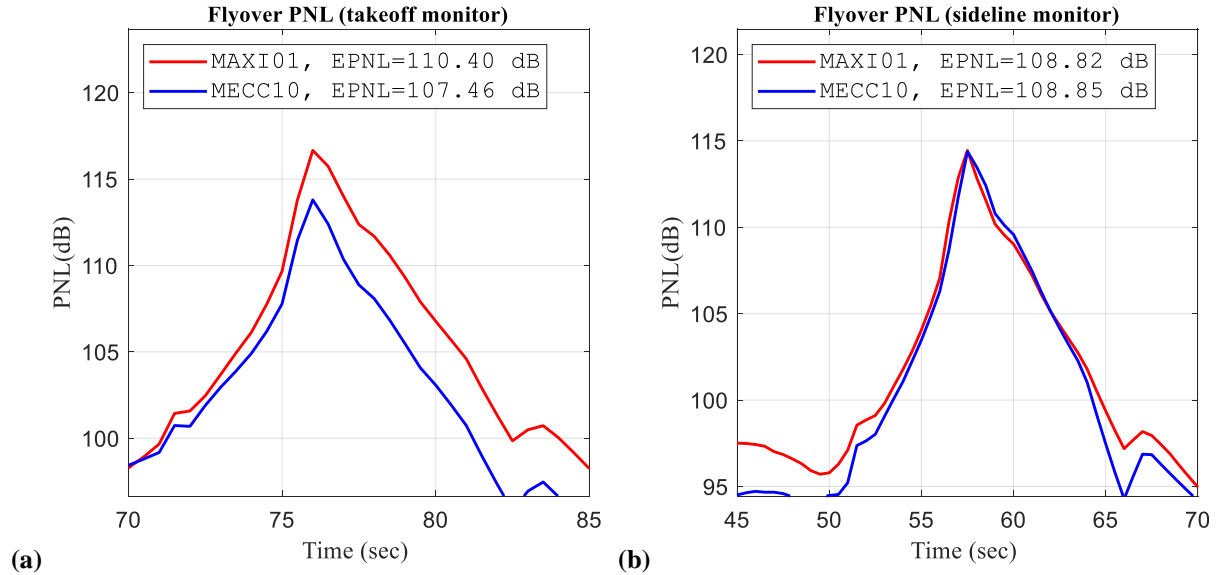


**Fig. 31 Experimentally-based estimates of flyover PNL history and EPNL for (a) takeoff minor and (b) sideline monitor. Red line: jet MAXI01 (baseline); Blue lines: jet MECC10 (optimal nozzle).**

### IX. Concluding Remarks

A framework was presented for the rapid acoustic optimization of three-dimensional, multi-stream nozzles for the propulsion of supersonic aircraft. It is based on Reynolds-Averaged Navier Stokes solutions combined with a Design of Experiments approach. The RANS flow field is collapsed to a surface, the OSPS, that is expected to contain the most important contributions to far-field sound emission. Differential noise predictions are achieved using a modified acoustic analogy, with emphasis on the change in effective perceived noise level (EPNL). Response surfaces for EPNL and thrust loss are obtained after parameterization of the nozzle geometry. The optimal configuration was tested experimentally and its reduction in cumulative EPNL was found to be within  $\sim 1$  dB of the predicted value of 3.8 dB.

The calibration of the predictive model was based on a limited set of existing experimental data. A larger number of baseline-modified pairs will be needed to increase the robustness of the model and verify its applicability over a range of operating conditions. The main cost of the prediction and optimization is that of the RANS computations. Given adequate resources and experience, this could be on the order of one day to compute  $\sim 10$  variations in geometry (in our case, computations for 10 cases took 5 days). The cost of computing the OSPS, and quantities on it, is modest – on the order of 10 minutes for each case. However, currently this computation cannot be done blindly and requires careful inspection of the results to ensure that spurious gradients do not result in an unphysical OSPS. Real-time visualization tools could assist the operator in this respect.

The Design of Experiments (DOE) approach for optimizing the nozzle geometry required variable transformations to create a design space compatible with DOE. Even though these transformations were specific to the nozzle deformations performed here, it is expected that other non-simple changes in geometry will likely require similar transformations.

### Acknowledgments

This work was completed with NASA Phase I and Phase II Small Business Innovation Research (SBIR) funding, contract 80NSSC18P1887, under technical monitor Dr. Brenda Henderson of NASA GRC. Spectral Energies, LLC, was the prime. Discussions with Dr. Sivaram Gogineni and Dr. Christopher

Ruscher of Spectral Energies are acknowledged. The following individuals are thanked for their contributions to the UCI effort: Dr. Juntao Xiong (RANS computations); Mr. Andres Adam (nozzle design); and Mr. David Morata (preparation and running of experiments).

## References

1. Bridges, J. and Wernet, M.P, “Validating Large-Eddy Simulation for Jet Aeroacoustics,” *Journal of Propulsion and Power*, Vol. 28, No. 2, 2012, pp. 226–234.
2. Bres, G.A., Ham, F.E., Nichols, J.W. & Lele, S.K 2017 “Unstructured Large-Eddy Simulations of Supersonic Jets,” *AIAA Journal*, Vol. 55, No. 4, 2017.
3. Lighthill, M.J., “On Sound Generated Aerodynamically: I. General Theory,” Proceedings of the Royal Society of London, Vol. 211, 1952, pp. 564–587.
4. Morris, P. J. and Farassat, F. “Acoustic Analogy and Alternative Theories for Jet Noise Prediction,” *AIAA Journal*, Vol. 40, No. 4, 2012, pp. 671–680.
5. Morris, P.J and Boluriaan, S., “The Prediction of Jet Noise from CFD data,” AIAA Paper 2004-2977, 2004.
6. Goldstein, M.E. and Leib, S.J., “The Aeroacoustics of Slowly Diverging Supersonic Jets”, *Journal of Fluid Mechanics*, Vol. 600, 2018, pp. 291–337.
7. Khavaran, A., Bridges, J.E., and Georgiadis, N., “Prediction of Turbulence-Generated Noise in Unheated Jets (Part 1: JeNo Technical Manual (Version 1))”, NASA/TM 2005-213827, 2005.
8. Khavaran, A., Wolter, J.D., and Koch D., “Prediction of Turbulence-Generated Noise in Unheated Jets (Part 2: JeNo Technical Manual (Version 1))”, NASA/TM 2009-231827, 2009.
9. Depuru Mohan, N.K. and Dowling, A.P., “Jet-noise-prediction model for chevrons and microjets”, *AIAA Journal*, Vol. 54, No. 12, 2016, pp. 3928–3940.
10. Khavaran, A. and Bridges, J., “An Empirical Temperature Variance Source Model in Heated Jets”, NASA/TM—2012-217743, 2012.
11. Leib, S.J., 2014 “Modeling Sound Propagation Through Non-Axisymmetric Jets”, NASA/CR–2014218107, 2014.
12. Goldstein, M. E., Sescu, A., and Afsar, M. Z., “Effect of Non-Parallel Mean Flow on the Green’s function for Predicting the Low-Frequency Sound from Turbulent Air Jets,” *Journal of Fluid Mechanics*, Vol. 695, Mar. 2012, pp. 199–234.
13. Henderson, B., Leib, S. and Wernet, M. “Measurements and Predictions of the Noise from Three-Stream Jets”, AIAA Paper 2015-3120, 2005.
14. Leib, S. J., Georgiadis, N. J., and Yoder, D. A., “Reynolds-Averaged Navier-Stokes Solutions and Noise Predictions for Three-Stream Jets,” AIAA Paper 2016-1882, 2016.
15. Papamoschou, D., “Modeling of Noise Reduction in Complex Multistream Jets,” *Journal of Fluid Mechanics*, Vol. 834, 2018, pp. 555-599.
16. Papamoschou, D., Xiong, J., and Liu, F., “Aerodynamics of Fan Flow Deflectors for Jet Noise Suppression,” *Journal of Propulsion and Power*, Vol. 24, No. 3, 2008, pp. 437-445.
17. Jameson, A., Schmidt, W., and Turkel, E., “Numerical Solutions of the Euler Equations by Finite Volume Methods Using Runge-Kutta Time Stepping Schemes,” AIAA Paper 1981-1259, January 1981.

18. Menter, F., "Two-Equation Eddy-Viscosity Turbulence Models for Engineering Applications," *AIAA Journal*, Vol. 32, No. 8, 1994, pp. 1598-1605.
19. Papamoschou, D., "Acoustic Simulation of Coaxial Hot Air Jets Using Cold Helium-Air Mixture Jets," *Journal of Propulsion and Power*, Vol. 23, No.2, 2007, pp. 375-381.
20. Bass, H., Sutherland, L., Blackstock, D., and Hester, D., "Atmospheric Absorption of Sound: Further Developments," *Journal of the Acoustical Society of America*, Vol. 97, No. 1, 1995, pp. 680-683.
21. Papamoschou, D. and Phong, V. "Perceived Noise Assessment of Offset Three Stream Nozzles for Low Noise Supersonic Aircraft," AIAA Paper 2018-1740, Jan. 2018.
22. "Noise Standards: Aircraft Type and Airworthiness Certification," Federal Aviation Regulations Pt. 36, Federal Aviation Administration, 2001.
23. Boeker, E.R., Dingles, E., He, B., Fleming, G., Roof, C., Gerbi, P., Rapoza, A., and Hemann, J., "Integrated Noise Model (INM) Version 7.0 Technical Manual," Federal Aviation Administration, Report FAA-AEE-08-01, January 2008.
24. Shanno, D.F. and Phua, K.H., "Minimization of Unconstrained Multivariate Functions," *ACM Transactions on Mathematical Software*, Vol. 2, No.2, 1976, pp. 87-94.
25. Papamoschou, D., "Engine Cycle and Exhaust Configurations for Quiet Supersonic Propulsion," *Journal of Propulsion and Power*, Vol.20, No.2, 2004.
26. Huff, D.L., Henderson, B.S., Berton, J.J., and Seidel, J.A., "Perceived Noise Analysis for Offset Jets Applied to Commercial Supersonic Aircraft," NASA/TM-2019-220049 (also AIAA-2016-1635).
27. Henderson, B., Norum, T., and Bridges, J., "An MDOE Assessment of Nozzle Vanes for High Bypass Ratio Jet Noise Reduction," AIAA Paper 2006-2543, May 2006.
28. Henderson, B. and Bridges, J., "An MDOE Investigation of Chevrons for Supersonic Jet Noise Reduction," AIAA Paper 2010-3926, June 2010.
29. Henderson, B. and Papamoschou, D., "A Design of Experiments Investigation of Offset Streams for Supersonic Jet Noise Reduction," AIAA Paper 2014-3739, July 2014.
30. McDonald, D.B., Grantham, W.J., Tabor, W.L., and Murphy, M.J., "Global and Local Optimization Using Radial Basis Function Response Surface Models," *Applied Mathematical Modeling*, Vol. 31, 2007, pp. 2095-2110.